Universitat Rovira i Virgili

Escola Tècnica Superior d'Enginyeria Química

Universidad Internacional de La Rioja

Escuela Superior de Ingeniería y tecnología

Máster Interuniversitario en Mecánica de Fluidos Computacional

Numerical Study of Wind Aerodynamics in a Low-Rise Industrial Building Using RANS Modelling

Trabajo fin de estudio presentado por:	ISMAEL MAJDOUBI GARCÍA
Tipo de trabajo:	SIMULACIÓN NUMÉRICA
Director/a:	FRANCISCO HUERA-HUARTE
Fecha:	14/07/2025

Abstract

Low-rise buildings, especially those used for industrial purposes, are highly exposed to wind-induced damage due to their large roof spans and limited anchoring structures, particularly in coastal and open-terrain areas. This master's thesis presents a numerical investigation into the aerodynamic behaviour of a stepped-roof industrial building subjected to realistic coastal Atmospheric Boundary Layer (ABL) wind conditions. The study uses Computational Fluid Dynamics (CFD) simulations, specifically a steady Reynolds-Averaged Navier-Stokes (RANS) approach with the RNG k–ε turbulence model and Enhanced Wall Treatment (EWT), validated through replication of a well-established benchmark study by Z. Liu et al. Initially, the numerical setup, including meshing strategies, turbulence modelling, and boundary condition definition with User Defined Functions (UDFs), was validated against the benchmark Large-Eddy Simulation (LES). Subsequently, this validated methodology was extrapolated to a realistic industrial-scale building, analysed at a significantly reduced scale ($1 : 1000$) due to computational constraints. Results highlight key aerodynamic phenomena such as velocity fields, surface pressure coefficient distributions, flow separation zones, recirculation regions, and vortex structures. The findings demonstrate the viability and accuracy of steady-state RANS simulations in capturing critical aerodynamic features, offering a computationally efficient method suitable for preliminary design phases in structural engineering and wind load assessments for industrial buildings.

Keywords: Low-Rise Buildings, Flow Topolgy, RANS, ABL.

Contents

List of Figures

List of Tables

Chapter 1

Introduction

Low-rise buildings are defined generally as structures with heights less than their plan dimensions, which are used for residential and industrial purposes. These types of structures constitute the majority of the global buildings. Due to their geometry (wide bases and relatively low height) these buildings are particularly vulnerable to wind-induced damage such as intense uplift forces in roofs, suction pressures at corners and roof edges and structural deformation during storms and hurricanes, particularly in coastal and open-terrain areas [1]. Post-disaster assessments, such as those following Hurricanes Dorian (2019) (see figure 1.1) and Laura (2020), have shown that a significant portion of wind-related losses are concentrated in low-rise residential and industrial constructions, especially those with large roof spans and limited anchoring [2], [3].

Figure 1.1: A photo taken after Hurricane Dorian in 2019 shows how the walls and roof of a one-story elevated house on Abaco Island were damaged by the storm [4]

The aerodynamic behaviour of wind interacting with low-rise and high-rise buildings can create complex pressure distributions and loads on the building configuration that must be considered for a safe structural design. When wind flows around structures, it produces stagnation points on the windward facade (see figure 1.2), along with turbulent flow separation at roof edges and sharp corners, yielding in highly unsteady recirculation regions, corner vortices, and strong pressure gradients. These are characterized by pressure coefficients (C_p), which can be defined as a non-dimensional parameter of how wind pressure varies over a surface that are influenced by the building geometry, wind profile, terrain roughness (location), and wind turbulence.

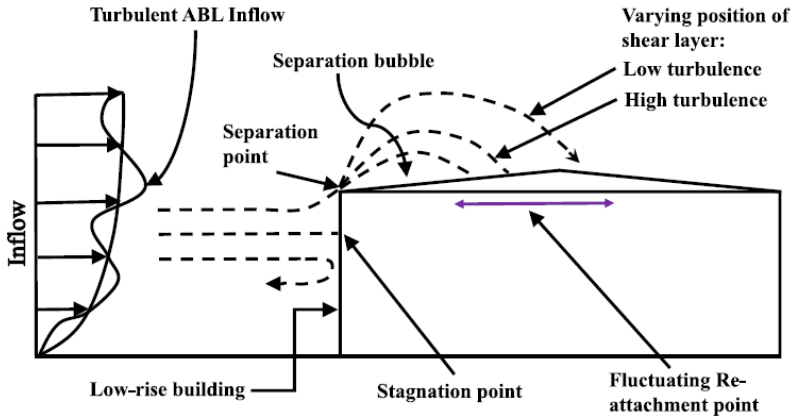

Figure 1.2: Wind flow pattern around a low-rise building represented with Atmospheric Boundary Layer [3]

The non-dimensional numbers involved in the physics of the problem can be reduced to the Reynolds number (Re):

$$Re = \frac{\rho V L}{\mu} \tag{1.1}$$

which characterizes the relationship between inertial forces and viscous forces in the flow [5] and Jensen number (Je):

$$Je = \frac{H}{\delta} \tag{1.2}$$

which defines the ratio between the characteristic height of the model and the roughness

length of the terrain [6].

Although there are many more dimensionless numbers such as Strouhal (vortex shedding frequency) or Mach (relationship between wind speed and sound speed), may influence certain aspects of flow, they are not critical for this study, which focuses on incompressible, subsonic external flow. As shown in figure 1.3, the flow topology around bluff bodies like low-rise buildings exhibits a range of aerodynamic features, such as shear layer detachment, recirculation, reattachment, and vortex shedding, all of which play a role in determining the resultant wind loads. These loads can translate into severe uplift and lateral forces on cladding, roof panels, and structural connections. The amount and distribution of pressures on a building will change over time due to the fact that real wind loads during a storm vary with time and space [7]. The shape of a building's roof also affects on how air flows around it and interact with the building [8].

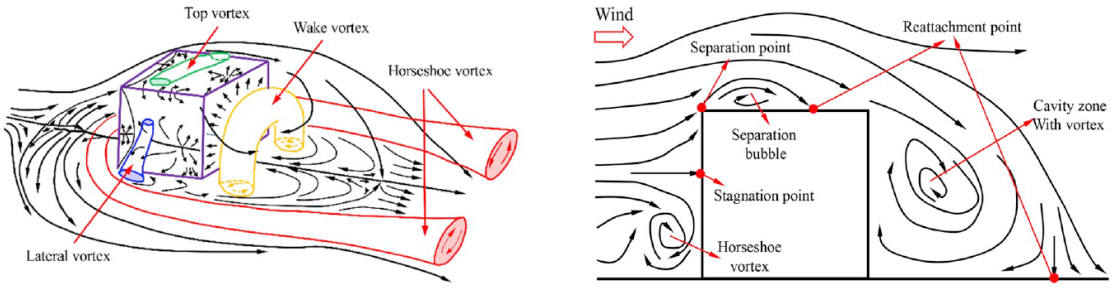

Figure 1.3: Flow topology scheme around a cubic obstacle [9]

Traditionally, wind loads can be evaluated with different methods: full-scale measurements, wind-tunnel tests using PIV measurements (scaled models) and computational fluid dynamics (CFD) simulations with corresponding benefits and drawbacks. There are differences between model-scale aerodynamic tests and full-scale experiments, particularly with regard to peak pressures. Two main causes of these disparities were identified in a number of papers as the inequality in Reynolds numbers and the absence of large-scale eddies in small-scale wind studies. The low energy content of the incident flow's large eddies and the high energy content of its small eddies are specifically the cause for the disparity in small-scale experimental predictions [10]–[12].

To better understand and mitigate the wind impact, the scientific community has advanced the use of CFD to simulate turbulent airflow around low-rise buildings. Techniques such as steady Reynolds-Averaged Navier-Stokes (RANS) and Large-Eddy Simulation (LES) have allowed researchers to predict pressure distributions, identify critical zones of aerodynamic load-

ing, and visualize complex flow structures such as vortex shedding, separation bubbles, and reattachment zones. Studies, such as Z. Liu et al. [9] combined PIV wind tunnel measurements with LES on varied roof geometries, validating that flat roofs tend to produce cleaner shear layers, while gable and stepped roofs induce multiple interacting vortices that require fine-scale resolution. While LES provides high fidelity, it also requires significant computational resources, motivating the development of hybrid approaches such as Detached Eddy Simulation (DES) and wall-modeled LES (WMLES) [3].

These aerodynamic analyses have a wide range of practical applications in structural engineering and building performance. CFD-based pressure maps help engineers refine design loads for wind-resisting systems beyond the simplifications assumed in codes like ASCE 7 or Eurocode 1. More specifically, they support local optimization of roof fasteners, cladding panels, and parapets, especially in industrial buildings with large roof areas. In urban planning, accurate airflow simulations help define wind comfort and safety criteria at pedestrian levels, while in energy efficiency design, they aid in improving natural ventilation strategies by predicting recirculation zones and cross-flow potential [8], [11]. Despite these advances, relevant gaps remain. Most high-fidelity LES and experimental studies are conducted at model scale $(1:100\text{–}1:500)$ and focus primarily on residential-scale buildings with conventional roof types (flat, gable). There is limited research on low-rise industrial buildings with flat, step and gable roofs, especially at moderate heights ($\sim 30\ m$). Moreover, many LES studies neglect full-scale atmospheric boundary layer (ABL) effects, and rely on idealized inflow conditions, which reduces their applicability to real-world design. Hybrid RANS-LES approaches, although promising in reducing computational costs, are still lacking standardized protocols for turbulence inflow generation, wall modelling, and grid sensitivity when applied to complex low-rise geometries [2], [3], [13].

This study is based directly on the investigation by Z. Liu et al. [9], which analysed wind flow over stepped and gable-roof models using LES and PIV. As a first step, we replicate their stepped-roof case using steady-state RANS in ANSYS Fluent, matching the inlet conditions and turbulence parameters: $U^*_{ABL} = 0.53\,m/s$, $y_0 = 2.04 \times 10^{-4}\,m$, and a target velocity of $U_{ref} = 7.4\,m/s$. It is going to be used a steady RANS approach due to computational constraints but incorporates a logarithmic velocity inlet profile representative of the coastal ABL (Tarragona). This allows for a direct comparison between RANS and LES in terms of flow topology, providing insight into the extent to which RANS can reproduce key aerodynamic features in complex low-rise configurations. On the other hand, this enables the feasibility of using RANS simulations, such as, to study pedestrian comfort as well as first steps in an

engineering project.

Once validated, this methodology is extrapolated to an industrial-scale building of realistic proportions ($200\ m \times 315\ m$ rectangular base and stepped roof with rectangular base reaching $32\ m$ total height), scaled to $1:1000$ due to computational limitations. While experimental data is unavailable for the new configuration, the geometric similarity and consistent modelling set-up justify the approach. Despite the extensive published works on bluff-body aerodynamics, several gaps persist that this study aims to address explicitly. Most previous CFD studies either focus on simplified cubes or residential-scale buildings, often neglecting industrial geometries of moderate height and large footprint, particularly under moderate building heights around 30–35 meters, where shear-layer interactions become sensitive to both geometry and turbulence content. Moreover, very few studies attempt to validate RANS simulations against LES results under matched ABL inputs and scaled setups. The literature also lacks examples of RANS implementation at extreme scale reductions ($1:1000$) with preserved turbulence structure and realistic boundary conditions. Most of the existing studies focus on simplified geometries (for instance, cubes, gable roofs) or residential scales, typically ranging between $1:100$ and $1:200$ [3], [9], [11].

By replicating a validated benchmark (Z. Liu et al. [9]) and applying it to a complex stepped-roof industrial building, this work offers an accessible methodology for early aerodynamic design in real-world engineering, especially where computational limitations prevent LES. This approach provides a replicable strategy for aerodynamic evaluation in design offices or early-stage engineering, where high-fidelity LES is often not feasible.

Therefore, the simulation's aim is to extract velocity fields, pressure coefficients, identify critical flow structures such as separation zones and recirculation regions in an industrial building of great dimensions with heights around 30–35 meters applying an extreme scale of $1:1000$, exposed to real coastal ABL profiles in a RANS approach. It is performed by previously validating the simulation setup with Z.Liu et al.'s [9] paper comparing the presented results.

Chapter 2

State of the art

This chapter outlines the main experimental and computational efforts to date and situates the present work within that context.

2.1 Aerodynamics of Low-Rise Buildings: Fundamentals and Key Differences

The interaction between wind and buildings is highly dependent on geometry, height-to-width ratio, and relationship with the atmospheric boundary layer (ABL). In general terms, buildings are classified as low-rise or high-rise, based on the ratio between height and plan dimensions. While high-rise buildings tend to trigger flow acceleration and vortex shedding governed by large-scale vertical structures, low-rise buildings exhibit early flow separation at roof edges and sharp corners, leading to the formation of recirculation zones, corner vortices, and peak suction regions that can cause critical structural loading.

However, notable gaps persist in the literature. Many high-fidelity studies neglect the influence of atmospheric turbulence structure at realistic coastal exposures; others focus on idealized cubes or gable roofs, omitting stepped industrial forms. Validation of RANS under scaled conditions ($1:500$–$1:1000$) is also sparse, particularly when targeting flow structures like roof-edge separation or corner vortices that are known to be Reynolds-sensitive.

This flow behaviour has been studied through three primary approaches: scaled wind tun-

nel experiments, full-scale open-jet testing, and computational fluid dynamics (CFD). However, the results depend strongly on Reynolds number, inflow turbulence spectra, and boundary conditions, making cross-study comparisons complex and underscoring the need for well-documented methodologies and validation datasets.

2.2 Experimental Studies: Validation Benchmarks and Reference Works

Experimental campaigns remain essential to validate CFD models and to understand key flow mechanisms in the vicinity of low-rise buildings. One of the most robust benchmark studies is that of Z. Liu et al. [9], who combined Particle Image Velocimetry (PIV) with LES simulations for flat, gable, and stepped roof geometries at $Re \sim 10^4$. Their analysis revealed a strong match between LES and PIV for mean velocity profiles ($\text{FAC}_2 > 0.9$), but second-order statistics (for instance, turbulent fluctuations) showed greater variance, especially near roof edges. These discrepancies suggest that while LES captures dominant flow structures, some finer turbulent details are sensitive to mesh density and experimental uncertainty.

At larger scales, Abdelfatah et al. [13] used a $1:10$ scale open-jet test facility to evaluate wind pressures on elevated residences. They compared these results with RANS simulations and found that while mean C_p values were generally within 10%, peak suctions were underestimated by up to 18% using standard wall functions. This supports the use of RANS for early design but highlights its limitations in capturing dynamic peak loads.

Mooneghi et al. [11] further investigated the impact of turbulence intensity and roof clearance, showing that LES in open-jet conditions replicates full-scale roof suction effects more accurately than traditional wind tunnel setups. Importantly, they found that scaling effects become significant at model scales below $1:200$, due to changes in flow separation behaviour and vortex interaction.

Additional studies have highlighted how poorly scaled inlet profiles and short fetch lengths can invalidate comparisons with real atmospheric flows. Montazeri and Blocken [14] demonstrated that pressure coefficients on windward faces can deviate by more than 20% if the inlet boundary layer is not fully developed, even with refined meshing. Blocken [15] reinforced this by emphasizing the necessity of proper turbulence intensity, inflow length, and boundary condition treatment to preserve aerodynamic similarity, especially when using small-scale models.

2.3 CFD Studies: From RANS to LES and Hybrid Approaches

The application of CFD to wind engineering problems involving low-rise buildings has advanced significantly in recent years, particularly due to the development of turbulence-resolving models such as Large Eddy Simulation (LES) and hybrid approaches that balance computational cost and fidelity. However, steady-state Reynolds-Averaged Navier–Stokes (RANS) models remain widely used in early-stage design due to their low computational requirements and acceptable performance in predicting mean flow characteristics. RANS methods solve the time-averaged Navier–Stokes equations, modelling the effects of turbulence through closures such as the realizable k–ε, standard k–ω, or SST k–ω models. These approaches can reliably predict bulk flow features, such as stagnation points, general recirculation zones, and mean wind pressures, especially when applied to simplified geometries. Several studies, such as Tominaga et al. [8], have reported that RANS models yield errors within 10–15% for mean pressure coefficients (C_p) on windward and leeward facades.

Additional comparative studies confirm the limited ability of RANS to capture complex transient dynamics in natural ventilation and internal flows. Shirzadi et al. [16] reported that steady RANS simulations correctly predicted mean pressure coefficients but failed to reproduce turbulent anisotropy and cross-ventilation dynamics that were captured by LES and wind tunnel experiments. Similarly, Van Hooff and Blocken [17] compared RNG k–ε and SST k–ω models against LES, concluding that while RANS approximated jet paths, it significantly underestimated turbulent kinetic energy, reducing accuracy in ventilation predictions.

However, RANS models are inherently limited in their ability to capture transient phenomena, such as vortex shedding, shear-layer instabilities, and unsteady pressure fluctuations that are critical in regions of flow separation, particularly at roof edges and corners. These unsteady mechanisms are responsible for peak suctions and dynamic loading, which are of great importance in structural design. As a result, RANS tends to underpredict peak suctions and produce overly diffuse wake regions unless very fine meshes and enhanced near-wall models are employed [2].

LES addresses these limitations by resolving the larger, energy-containing eddies directly, while modelling only the smaller, subgrid-scale (SGS) turbulence using appropriate SGS models (for instance, Smagorinsky–Lilly, dynamic Smagorinsky, or WALE). LES enables accurate representation of unsteady flow structures, such as coherent vortices and turbulent shear layers, making it well suited for analysing wind loading on bluff bodies. For instance, in the study by

Haines and Taylor [18], LES was employed to investigate the aerodynamic response of low-rise buildings under transient downburst events, a particularly severe form of wind loading characterized by radial outflows and impulsive gusts. The LES model captured the development of conical vortices and highly unsteady, asymmetric pressure fields that would be impossible to resolve with RANS. Haines and Taylor demonstrated that LES could reproduce dynamic uplift forces and vortex-induced lateral loads, which are critical for assessing structural safety during non-synoptic wind events. The selection of SGS models plays a critical role in LES accuracy. For instance, while the WALE model performs well near walls, the Smagorinsky–Lilly model can lead to excessive damping of vortical structures unless dynamically adjusted, especially in coarse grid scenarios [19]. A benchmark by Lübcke et al. [20] compared LES and RANS predictions of unsteady wake flows behind bluff bodies. They observed that even with advanced stress transport models, RANS could not resolve vortex shedding or capture the time-varying wake structure, highlighting the need for eddy-resolving models when investigating unsteady aerodynamic loads.

Similarly, Mooneghi et al. [11] used LES in an open-jet wind tunnel setup to study the effects of turbulence scale and roof geometry on flow separation in low-rise structures. Their findings confirmed that LES provides superior resolution of transient flow behaviour, but also highlighted the computational intensity of such simulations, requiring tens of millions of cells and fine time-step resolution to ensure convergence.

To mitigate the computational cost of wall-resolved LES, especially in high Reynolds number simulations, researchers have proposed hybrid models, such as Detached Eddy Simulation (DES) and its more advanced form, Improved Delayed Detached Eddy Simulation (IDDES). These approaches use RANS modelling in the near-wall region (where mesh requirements are otherwise extreme) and switch to LES in the outer, separated flow zones. This makes them particularly suitable for complex building geometries, where both accuracy in recirculation zones and computational efficiency are required. In their comprehensive review, Khaled and Aly [3] evaluated multiple hybrid modelling strategies applied to low-rise structures. Their study compared the performance of steady RANS, LES, and IDDES against benchmark experimental data. They found that while steady RANS underestimates peak suctions and smooths out dynamic wake behaviour, IDDES can predict pressure coefficients within 10% of wind tunnel results, with less than 50% of the computational demand of wall-resolved LES. Additionally, they emphasized the need for accurate inflow turbulence generation, recommending the use of synthetic eddy methods (SEM) or precursor simulations to ensure realistic turbulence profiles at the domain inlet. However, they noted the absence of standardized procedures for

mesh transition, wall-model calibration, and SGS parameter tuning, especially for cases involving sharp-edged, bluff body flows like industrial low-rise buildings. Nonetheless, Larsson and Wang [21] caution that hybrid methods lack full standardization, particularly in mesh transition regions and subgrid parameter tuning for complex flows, suggesting that careful calibration is still necessary.

Khaled et al. [22] further advance the assessment of modelling fidelity by conducting a systematic comparison of steady RANS, wall-resolved LES, and hybrid RANS–LES (specifically IDDES) on the canonical Silsoe cube geometry. They employed a multi-scale approach, spanning model scales of $1:10$ to near-full scale, to evaluate the sensitivity of predicted C_p to inflow turbulence specification, mesh refinement, and wall treatment. Their findings indicate that while RANS can reproduce mean C_p distributions within 15% of wind-tunnel data, it fails to capture instantaneous suction peaks exceeding $C_p = -2.0$. In contrast, wall-resolved LES accurately predicts these peak loads ($\pm 5\%$ error) but incurs computational costs an order of magnitude higher. Importantly, the IDDES hybrid method delivers a compromise: it achieves peak C_p errors within 10% using approximately 40% fewer cells than LES, provided that synthetic eddy inflow is implemented and mesh stretching near walls is minimized. These results underscore the potential of hybrid models for industrial low-rise applications, while also emphasizing the need for carefully calibrated inflow and wall models when operating at reduced scales.

A recurring limitation in both experimental and numerical investigations is the dependence on geometrically scaled models (typically $1:100$ to $1:1000$) to reduce cost and domain size. However, aerodynamic similarity is not guaranteed at small scales due to Reynolds number effects. For instance, roof-edge separation bubbles and vortex shedding patterns are known to be Re sensitive, and their development can be delayed or suppressed in low-Re conditions, leading to underestimation of dynamic loads [3]. Moreover, turbulence generation in wind tunnels is often limited by blockage ratios and fan array resolution, which means that inflow turbulence intensity and integral length scales are not always representative of atmospheric flows. These limitations also apply to CFD simulations at reduced scales unless explicit synthetic turbulence is introduced at the inlet (as shown in Tominaga et al. [8]; Abdelfatah et al. [13]). As such, care must be taken when extrapolating small-scale CFD results to full-scale behaviour.

Building on the challenges of small-scale modelling highlighted by Khaled and Aly [3], additional studies reinforce the difficulty of achieving aerodynamic similarity when reducing model size. Montazeri et al. [14] demonstrated that truncated inflow fetch in wind tunnels leads to underdeveloped boundary-layer profiles, yielding C_p errors up to 20% on facade sur-

faces compared to full-scale data. Tominaga et al. [8] further showed that without synthetic turbulence generation, LES at $1:200$ scale fails to reproduce the integral length scales responsible for large-eddy interaction, causing delayed separation and underprediction of peak roof suctions by 15–30%. Abdelfatah et al. [13] confirmed this in open-jet experiments, where a $1:10$ elevated residence model exhibited 25% higher corner pressures under full-scale Reynolds numbers than in conventional tunnel tests. Meanwhile, Aly and Gol-Zaroudi [23] found that wall-modeled LES at $1:100$ scale required careful adjustment of SGS constants to match field observations of mono-pitch roofs, with improper calibration leading to over-smoothed vortex cores and C_p deviations of 10%. Collectively, these results underscore that mesh resolution, inflow turbulence characterisation, and SGS model selection are all scale-dependent and must be explicitly validated. As also emphasized by Blocken [15], improper application of CFD in low-Reynolds or short-fetch setups can lead to fundamentally incorrect conclusions regarding flow reattachment, vortex formation, and suction peaks, especially for sharp-edged geometries.

Finally, Blocken [24] emphasized that even advanced CFD simulations can yield unreliable predictions when turbulence generation, near-wall modelling, and domain size are not properly set, particularly at extreme scales. This reinforces the importance of systematic validation.

In summary, while RANS remains an essential tool for preliminary aerodynamic analysis, LES and hybrid models offer a path toward greater accuracy in simulating unsteady flow phenomena, particularly around low-rise buildings with complex geometries. The cost-benefit balance between model fidelity and computational feasibility continues to guide the selection of turbulence modelling strategies, with wall-modelled LES and IDDES emerging as strong candidates for future design-focused studies, provided that methodological standardization and validation efforts continue to mature. This study addresses these gaps by evaluating a $1:1000$ industrial low-rise geometry within a RANS framework, systematically quantifying the extent to which such a reduced-scale approach can replicate key flow features and pressure distributions documented in higher-fidelity LES and experimental benchmarks.

2.4 Summary of Other Studies

A selection of relevant experimental and CFD studies on low-rise building aerodynamics is summarised below in Table 2.1. These works cover a range of CFD and experimental methodologies, building geometries, and flow conditions. The table highlights how different strategies

(RANS, LEs and hybrid approaches) capture key aerodynamic phenomena. Several of these studies serve as direct references for the present work.

In light of the reviewed studies, the present work is positioned to complement and extend existing knowledge by applying validated RANS-based methods to a realistic industrial geometry under a highly reduced scale, while preserving key ABL features.

Table 2.1: Summary of Selected CFD and Experimental Studies on Low-Rise Building Aerodynamics

Study	**Main Features**	**Key Parameters**
Z. Liu et al. [9]	LES validated with PIV on flat, gable, and stepped roofs. Good agreement for mean velocity.	Scale: $1:200$, $Re \sim 10^4$; WALE model; Mesh: 8M cells; $\text{FAC}_2 > 0.9$ for $\bar{U}$
Haines & Taylor [18]	LES of downburst winds; resolved conical vortex and transient peak loads on cube.	Scale: $1:200$, $Re \sim 1.5 \times 10^4$; Unsteady jet profile; Captured uplift and lateral loads
Aly & Gol-Zaroudi [23]	Full-scale LES on mono-pitch industrial roof; compared to wind tunnel and field.	Full scale, $Re \sim 10^7$; Validated LES with experimental data; mono-pitch configuration
Khaled & Aly [3]	Comparison of IDDES and WM-LES; benchmark cube; synthetic turbulence inflow.	Scale: $1:100$, $Re \sim 10^4 - 10^5$; IDDES within 10% of wind tunnel data; 50% fewer cells vs. LES
Mooneghi et al. [11]	LES in open-jet tunnel; studied turbulence and clearance effects on roof suctions.	Scale: 1:100, $Re \sim 5 \times 10^5 - 10^6$; Peak C_p up to 25% higher than small-tunnel values
Khaled et al. [22]	RANS, LES, and IDDES applied to Silsoe cube; tested wall models and inflow conditions.	Scale: 1:10, $Re \sim 10^5$; LES better matches C_p with correct inflow; evaluated wall treatment
Montazeri & Blocken [14]	RANS validation with pressure taps; tested mesh dependence and inflow fetch in building corner flows.	Scale: $1:400$, $Re \sim 3 \times 10^5$; CFD–experiment error $< 15\%$ with corrected ABL input
Blocken [24]	Review on CFD reliability in urban aerodynamics; highlighted limitations from improper boundary setup.	Various scales; Emphasis on inlet length, turbulence spectra, and wall treatment calibration

Chapter 3

Numerical Setup and Validation

As reviewed in the previous Chapter, particularly in Section 2.3, the selection of a CFD modelling strategy must balance accuracy with computational feasibility. LES and hybrid models such as IDDES have shown strong performance in resolving unsteady aerodynamic structures in low-rise building flows [3], [9], [11], [13], [16], [18]. However, given the computational demands, a steady RANS approach has been selected for this work. The numerical simulations were performed with ANSYS Fluent version 2023 R1. The following sections set out the basics for the performed simulations.

3.1 Numerical Modelling Approach

Ansys Fluent follows a tree structure for defining the parameters of the simulation. It is divided in three major sections. **Setup** section is where the initial conditions, cell zone and boundary conditions are defined. Similarly, in **Solution** section the discretization methods, monitors, convergence criteria and simulation execution are placed. Finally, the results can be viewed in the **Results** section. Here all kind of plots, contours and animations are used to draw conclusions. The choice of turbulence model and numerical schemes is further justified in following sections for the intended replication and industrial extrapolation objectives.

3.1.1 Governing Equations: Turbulence Model Setup

The CFD simulations are based on the Reynolds-Averaged Navier–Stokes (RANS) equations for incompressible flow. These equations, which describe the conservation of mass and momentum, are given as:

$$\frac{\partial u_i}{\partial x_i} = 0, \qquad \rho\left(\frac{\partial u_i}{\partial t} + u_j\frac{\partial u_i}{\partial x_j}\right) = -\frac{\partial p}{\partial x_i} + \mu\frac{\partial^2 u_i}{\partial x_j^2} - \rho\frac{\partial \overline{u_i' u_j'}}{\partial x_j}, \tag{3.1}$$

where $\overline{u_i' u_j'}$ denotes the Reynolds stresses, which are modelled using the $k-\varepsilon$, $k-\omega$ or SST $k-\omega$ closures. These models include additional terms to account for the effects of turbulence and flow separation in the computational domain.

ANSYS Fluent 2023 R1 employs the Finite Volume Method (FVM) to discretize the governing equations. In ANSYS Fluent, various turbulence models are available for closing the Reynolds stress term $\overline{u_i' u_j'}$ in the RANS equations. Among the most widely used are the two-equation models, which solve transport equations for the turbulent kinetic energy k and a turbulence dissipation rate ε [25].

1. **Standard k–ε model:**

   This model solves transport equations for the turbulent kinetic energy k and the turbulent dissipation rate ε. It is robust and computationally efficient but assumes isotropic turbulence and performs poorly in regions of strong curvature or separation [25]. The model equations are:

$$\frac{\partial(\rho k)}{\partial t} + \frac{\partial(\rho k u_j)}{\partial x_j} = P_k - \rho\varepsilon + \frac{\partial}{\partial x_j}\left[\left(\mu + \frac{\mu_t}{\sigma_k}\right)\frac{\partial k}{\partial x_j}\right] \tag{3.2}$$

$$\frac{\partial(\rho \varepsilon)}{\partial t} + \frac{\partial(\rho \varepsilon u_j)}{\partial x_j} = C_{1\varepsilon}\frac{\varepsilon}{k}P_k - C_{2\varepsilon}\rho\frac{\varepsilon^2}{k} + \frac{\partial}{\partial x_j}\left[\left(\mu + \frac{\mu_t}{\sigma_\varepsilon}\right)\frac{\partial \varepsilon}{\partial x_j}\right] \tag{3.3}$$

2. **RNG k–ε model:**

   The Renormalization Group (RNG) variant improves accuracy in high-strain, swirling, and separated flows. It modifies the ε-equation by including an additional term R_ε that accounts for interaction between turbulence dissipation and strain. It is more suitable than the standard model for external flows with curvature and recirculation [25]. The

equations are:

$$\frac{\partial(\rho k)}{\partial t} + \frac{\partial(\rho k u_j)}{\partial x_j} = P_k - \rho\varepsilon + \frac{\partial}{\partial x_j}\left[\left(\mu + \frac{\mu_t}{\sigma_k}\right)\frac{\partial k}{\partial x_j}\right] \tag{3.4}$$

$$\frac{\partial(\rho\,\varepsilon)}{\partial t} + \frac{\partial(\rho\,\varepsilon\,u_j)}{\partial x_j} = C_{1\varepsilon}\,\frac{\varepsilon}{k}\,P_k - C_{2\varepsilon}\,\rho\,\frac{\varepsilon^2}{k} + R_\varepsilon + \frac{\partial}{\partial x_j}\left[\left(\mu + \frac{\mu_t}{\sigma_\varepsilon}\right)\frac{\partial \varepsilon}{\partial x_j}\right] \tag{3.5}$$

where $R_\varepsilon = C_\mu \rho \eta^3 \left(1 - \frac{\eta}{\eta_0}\right)\frac{\varepsilon^2}{k}$ and $\eta = Sk/\varepsilon$.

3. **Realizable k–ε model:**

   Designed to improve predictions for complex flows with large strain rates and streamline curvature. It replaces the standard ε equation and uses a variable C_μ [25]. The equations are:

$$\frac{\partial(\rho k)}{\partial t} + \frac{\partial(\rho k u_j)}{\partial x_j} = P_k - \rho\varepsilon + \frac{\partial}{\partial x_j}\left[\left(\mu + \frac{\mu_t}{\sigma_k}\right)\frac{\partial k}{\partial x_j}\right] \tag{3.6}$$

$$\frac{\partial(\rho\varepsilon)}{\partial t} + \frac{\partial(\rho\varepsilon u_j)}{\partial x_j} = \rho C_1 S\varepsilon - \rho C_2 \frac{\varepsilon^2}{k + \sqrt{\nu\varepsilon}} + \frac{\partial}{\partial x_j}\left[\left(\mu + \frac{\mu_t}{\sigma_\varepsilon}\right)\frac{\partial \varepsilon}{\partial x_j}\right] \tag{3.7}$$

   where $S = \sqrt{2S_{ij}S_{ij}}$ is the strain rate magnitude.

4. **k–ω and SST k–ω models:**

   These models solve transport equations for k and the specific dissipation rate $\omega = \varepsilon/(\beta^* k)$. The SST model combines k–ω near walls and k–ε in the far field using blending functions [25]. The base equations are:

$$\frac{\partial(\rho k)}{\partial t} + \frac{\partial(\rho k u_j)}{\partial x_j} = P_k - \beta^* \rho k\omega + \frac{\partial}{\partial x_j}\left[(\mu + \sigma_k \mu_t)\frac{\partial k}{\partial x_j}\right] \tag{3.8}$$

$$\frac{\partial(\rho\omega)}{\partial t} + \frac{\partial(\rho\omega u_j)}{\partial x_j} = \alpha\frac{\omega}{k}P_k - \beta\rho\omega^2 + \frac{\partial}{\partial x_j}\left[(\mu + \sigma_\omega \mu_t)\frac{\partial \omega}{\partial x_j}\right] \tag{3.9}$$

   In SST, the production term is limited and transport coefficients are blended depending on wall distance.

While LES offers greater accuracy, particularly in resolving unsteady vortices and dynamic loads [9], [11], [18], the computational cost is substantially higher, often by a factor of 80 to 100 compared to steady RANS [16], [17]. Hybrid models such as IDDES have shown promising

results, as demonstrated by Khaled and Aly [3], but still require careful handling of turbulence inflow and near-wall regions.

Given the need to perform multiple simulations and the lack of access to high-performance computing clusters, the steady RANS approach with RNG k–ε and Enhanced Wall Treatment (EWT) and pressure gradient effects offer a well-balanced compromise. This model allows the study to capture the primary flow characteristics, such as velocity fields, stagnation zones, and mean pressure distributions, with reasonable accuracy, while maintaining computational feasibility. It provides better predictions than the standard variant in regions with flow separation and adverse pressure gradients, which are characteristic of the roof-edge and wake dynamics in low-rise buildings.

3.1.2 Meshing

The mesh is a discretized representation of the physical domain, essential in numerical simulations of CFD, as it directly influences the accuracy, stability, and convergence of the results [26]. Fluent Meshing, part of the Ansys software package, integrates tools such as Space Claim for geometry modifications and provides a "watertight geometry" option for synchronized CAD models. Various mesh types can be used depending on the geometry(see figure 3.1): tetrahedral meshes for complex shapes, hexahedral meshes for simpler geometries or aligned flows, and polyhedral meshes to enhance overall quality. Mesh quality is critical and is evaluated through metrics such as element size, aspect ratio, skewness, orthogonality, and volume, with optimal values minimizing distortion and maximizing alignment with the geometry. Tools like *Add Local Sizing* allow refinement in specific regions, especially using *Body of Influence*, to improve accuracy in critical fluid areas. The surface mesh generation process discretizes the solid's surface, typically defaulting to a hexahedral mesh, and requires correctly defining whether the domain is a fluid volume, a fluid volume with voids, or a solid from which the control volume will be extracted. Finally, the addition of boundary layers becomes relevant in turbulent flows or when high wall-precision is needed, though it increases computational cost, making it essential to balance accuracy and efficiency.

An essential parameter to quantify whether the near-wall mesh is appropriate is the dimensionless wall distance, y^+, which indicates how well the viscous sublayer and buffer layer are resolved. In this context, and considering that the RNG k–ε turbulence model with EWT has been selected, the following details the role and calculation of y^+, as well as the mesh design

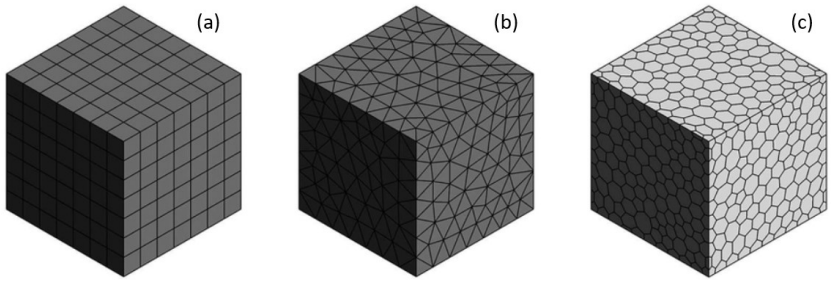

Figure 3.1: Types of meshes [27]

requirements it imposes.

The dimensionless wall coordinate, y^+, can be defined as:

$$y^+ = \frac{u_\tau y}{\nu}, \tag{3.10}$$

where $u_\tau = \sqrt{\tau_w/\rho}$ is the friction velocity, τ_w is the wall shear stress, y is the distance from the wall to the first cell centre, and ν is the kinematic viscosity of the fluid. This parameter quantifies the relative location of the first grid point with respect to the wall in terms of viscous units.

For accurate turbulence modelling near walls, different turbulence models impose different y^+ requirements:

- **Standard Wall Functions (SWF):** Require $30 < y^+ < 300$. The first grid point lies in the logarithmic region of the boundary layer.
- **Low-Re models or Wall-Resolved LES:** Require $y^+ \lesssim 1$, which resolves the viscous sublayer directly.
- **Enhanced Wall Treatment (EWT):** Can handle both low and high y^+ values by blending viscous and logarithmic models, but for best accuracy it is recommended to maintain $y^+ \approx 1$ [25].

Lastly, when selecting the *Generate Volume Mesh* operation, the choice of element type is critical. In this case, a **poly-hexcore** strategy was selected rather than a purely polyhedral mesh, for the following reasons:

- **Layered near-wall refinement:** Poly-hexcore allows the automatic generation of prism layers adjacent to wall boundaries, enabling the enforcement of $y^+ < 1$. This is essential for EWT, which is more robustly achieved with poly-hexcore than with fully polyhedral meshes.
- **Core efficiency and alignment:** The structured hexahedral core aligns with the primary flow direction, reducing numerical diffusion and enabling efficient resolution of the flow field. Compared to fully polyhedral meshes, poly-hexcore generally achieves the same accuracy with fewer cells in the core region.
- **Superior element quality:** By transitioning smoothly between the hexcore and polyhedral regions, the mesh maintains favourable quality metrics such as low skewness and high orthogonality. This improves numerical stability and accelerates convergence.

For these reasons, including better near-wall resolution, improved efficiency, superior quality metrics, and ease of setup, a **poly-hexcore mesh** was selected as the final meshing strategy for this study. Since the RNG k–ε model with EWT is used, a wall-resolved approach is adopted. Therefore, the mesh is refined in the near-wall region to maintain $y^+ \sim 1$ in the first cell layer, enabling the correct resolution of viscous effects and near-wall gradients. This requirement was verified during the mesh generation process.

3.1.3 Computational Domain

The computational domain's dimensions are crucial for ensuring that the numerical solution is not influenced by boundary interference. Different guidelines exist regarding the optimal sizing of domains for CFD simulations in wind engineering. Tominaga et al. [28] suggest minimum dimensions of $5H$ upstream, $10H$ downstream, $5H$ laterally, and $5H$ vertically, where H is the characteristic building height. Franke et al. [29], however, provide more conservative recommendations, proposing at least $5H$ upstream, $15H$ downstream, $6H$ vertically, and a minimum of $5H$ laterally. Recent studies such as Abu-Zidan et al. [30] have further explored the sensitivity of results to reduced domain sizes, finding that smaller computational domains can significantly impact flow development, pressure distributions, and flow separation characteristics. Notably, Z. Liu et al. [9] adopted a computational domain considerably larger than those recommended by Tominaga et al. and Franke et al., specifically extending further downstream and vertically, aiming to minimize boundary interference effects and fully capture the wake development and vortical structures downstream of the building. Abu-Zidan et al.

additionally highlighted that reductions in domain size notably influence velocity profiles and flow separation points, particularly in areas downstream of the building, reinforcing the conservative approach used here. For this reason, the present work follows strictly to the guidelines by Franke et al., ensuring reliable results. Figure 3.2 illustrates the computational domain employed by Jagbir Singh et al. [31] extracted from Franke et al., from which the dimensions for this work are referenced.

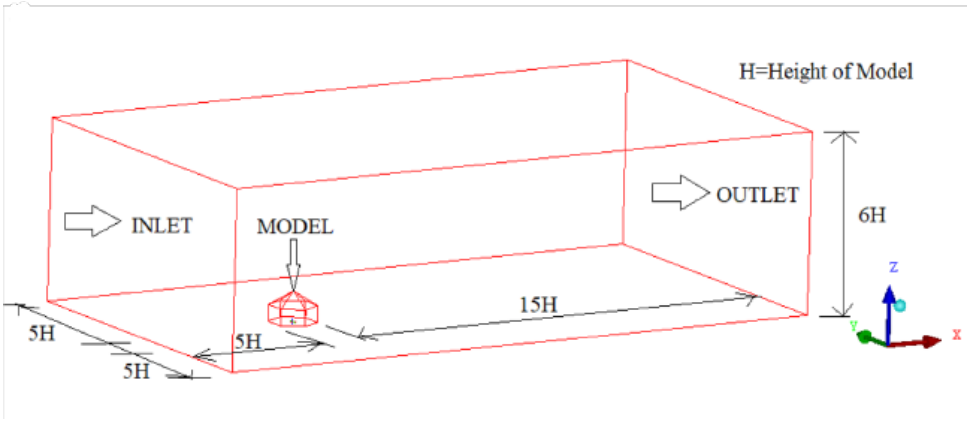

Figure 3.2: Computational domain example using the recommended guidelines [31]

Additionally, the blockage ratio, defined as the ratio of the building's frontal area to the total inlet area, should be kept below 5% to avoid significant interference effects, as recommended by Choi et al. [32]. Choi et al. investigated the influence of blockage ratio in wind tunnel experiments for buildings, highlighting that a blockage ratio under approximately 5% significantly reduces wall-induced interference on aerodynamic parameters such as wind pressures and flow structures, ensuring minimal deviation from real atmospheric conditions. This ratio is computed as:

$$\text{Blockage Ratio} = \frac{A_{\text{building}}}{A_{\text{inlet}}} \times 100\% \tag{3.11}$$

where A_{building} is the frontal area of the building and A_{inlet} the cross-sectional area of the inlet.

3.1.4 Boundary Conditions and Atmospheric Profile

The characteristics of boundary conditions (BC), particularly the inflow boundary representing the Atmospheric Boundary Layer (ABL), significantly influences the accuracy and reliability of CFD simulations in wind engineering. Accurate representation of atmospheric inflow is

essential because it dictates the initial state of turbulence and velocity distribution entering the computational domain, subsequently affecting the aerodynamics around structures. Hence, careful consideration and selection of inflow conditions and associated parameters based on empirical and theoretical guidelines is crucial.

At the inlet, a logarithmic velocity profile is applied to represent the ABL. This approach follows the methodology proposed by Richards and Hoxey [33] and further validated by Blocken et al. [34], who emphasize its suitability for simulating wind profiles typically observed in the lower atmosphere. Cochran [35] highlights that the structure, magnitude, and characteristics of the ABL strongly depend on local topographic and roughness features, emphasizing that the logarithmic profile parameters, such as friction velocity U^*_{ABL} and roughness length y_0, must be carefully selected to reflect realistic local atmospheric conditions. Particularly, Cochran demonstrates significant variations in wind speed profiles and turbulence intensities between coastal (this study, Tarragona), urban, suburban, and open-country exposures (as seen in figure **??**), underscoring the importance of accurate inlet boundary specification for reliable CFD simulations in wind engineering. The logarithmic law effectively describes how wind velocity increases logarithmically with height due to frictional effects at the Earth's surface, characterized by surface roughness elements and turbulence structure. The velocity profile is mathematically defined as:

$$U(z) = \frac{U^*_{ABL}}{\kappa} \ln\left(\frac{y + y_0}{y_0}\right) \tag{3.12}$$

where U^*_{ABL} is the friction velocity in m/s, a parameter representing the shear stress at the surface and determining the slope of the velocity profile; κ is the von Kármán constant typically ranging between 0.40 and 0.42 (often taken as 0.41); and y_0 is the aerodynamic roughness length, representing the height above ground at which the velocity theoretically becomes zero due to surface friction and roughness elements. U^*_{ABL} is often calculated a specified velocity at a reference height h:

$$U^*_{ABL} = \frac{\kappa U_h}{ln((h + y_0)/y)} \tag{3.13}$$

Additionally, turbulent kinetic energy (k) and turbulence dissipation rate (ε) profiles, consistent with the logarithmic velocity distribution, are defined as follows [33], [34]:

$$k = \frac{U^{*2}_{ABL}}{\sqrt{C_\mu}} = 3.33 U^{*2}_{ABL}, \quad \varepsilon = \frac{U^{*3}_{ABL}}{\kappa(y + y_0)} \tag{3.14}$$

with $C_\mu = 0.09$. Equations 3.12, 3.13, 3.14 presume that the computational domain's height remains significantly below the full atmospheric boundary layer height, as the hypothesis of uniform shear stresses holds true primarily within the lower region of the atmospheric boundary layer. In figure 3.3 can be seen the aforementioned profiles in different terrains and topographic conditions.

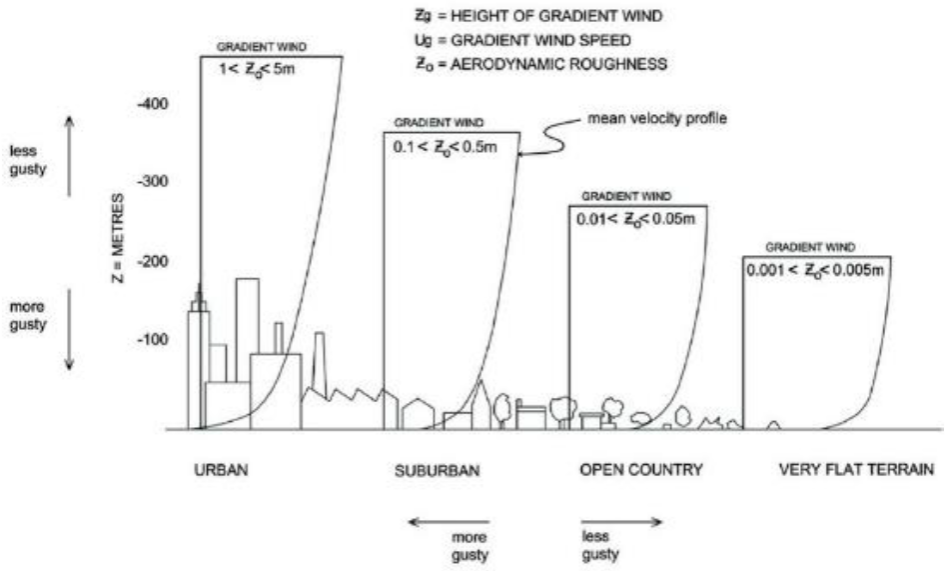

Figure 3.3: ABL variation according to topography [35]

These boundary conditions ensure turbulence characteristics accurately reflect the atmospheric surface layer. They are essential for maintaining flow stability and homogeneity throughout the computational domain, thereby avoiding artificial velocity gradients and ensuring realistic pressure distributions downstream [32]–[34].

To implement the desired atmospheric conditions within ANSYS Fluent, a User Defined Function (UDF) was developed. A UDF is a custom-written code that extends Fluent's built-in capabilities, allowing users to define specific boundary conditions, source terms, or fluid properties not directly available in the standard software package. In this study, the UDF was written in C programming language, following Fluent's recommended structure and syntax [25]. The code specifies a logarithmic velocity profile, turbulent kinetic energy, and turbulence dissipation rate at the inlet boundary, based on equations from Richards and Hoxey [33]. After compiling the UDF within Fluent, it was loaded into the simulation setup, enabling precise control of the inlet conditions and ensuring the correct atmospheric boundary layer characteristics throughout the computational domain. This method significantly enhances the accuracy and

realism of the simulation. The detailed UDF script is included in the Appendix A for further reference. Prior to simulations involving the building geometry, the inlet profiles were validated through preliminary simulations conducted in an empty computational domain to verify the horizontal homogeneity and consistency of the imposed atmospheric boundary layer conditions, following best practices in CFD validation recommended by some relevant authors.[24], [28], [29].

The boundary conditions used in the numerical domain are summarized as follows:

- **Inlet**: Velocity-inlet boundary condition is applied the logarithmic profiles for velocity, turbulent kinetic energy (k), and turbulence dissipation rate (ε).
- **Outlet**: Pressure-outlet condition with a zero-gauge pressure reference, ensuring the absence of artificial pressure gradients.
- **Building wall**: Described as no-slip wall boundary which is going to be a control surface to compute C_p and y^+ among other variables.
- **Ground wall**: Modelled as a rough wall; however, due to the application of Enhanced Wall Treatment, no explicit roughness height was assigned to maintain model consistency and numerical stability.
- **Top and lateral walls**: Defined as a wall with slip (symmetry) boundary condition to avoid artificial constraints on the flow and accurately represent the unbounded atmospheric conditions, following established recommendations by Blocken et al. [34].

The working fluid in all simulations is air, modelled as an incompressible, Newtonian fluid with constant thermophysical properties. The density was set to $\rho = 1.225\, kg/m^3$ and the dynamic viscosity to $\mu = 1.7894 \times 10^{-5}\, Pa \cdot s$, corresponding to standard atmospheric conditions at sea level and $15°C$. These values are consistent with the assumptions in previous CFD studies of external building aerodynamics and ensure compatibility with the turbulence model and wall treatment approach employed.

Furthermore, since both the geometry of the building and the computational domain are symmetric, a vertical symmetry plane was placed along the longitudinal axis. This reduces computational demands significantly, approximately dividing by two the required computational resources, without substantially compromising the accuracy of the results. Blocken et al. [24] support the use of symmetry planes in CFD simulations when studying symmetric buildings, particularly when the wind direction aligns closely with the symmetry plane. Montazeri

and Blocken [14] also confirmed through their research that symmetry conditions are reliable and efficient for aligned flows. However, it is important to recognize some limitations when applying symmetry conditions specifically within steady RANS simulations. Because the RANS methodology averages turbulence fluctuations to yield mean flow fields, applying a symmetry plane generally does not reduce the accuracy for mean velocity and pressure predictions, as validated by previous studies [14], [24]. Nevertheless, using symmetry means that any subtle asymmetric features arising from instantaneous turbulent fluctuations, typically captured by more computationally demanding methods such as LES, cannot be represented. Still, considering the primary goal here is to accurately capture time-averaged flow characteristics under conditions of aligned wind incidence, employing a symmetry boundary is both appropriate and beneficial, aligning with standard CFD practices.

In conclusion, the boundary conditions, atmospheric inlet profile, domain dimensions, blockage ratio, and symmetry plane adopted in this study align with best practices in CFD for wind engineering applications, ensuring accurate and computationally efficient simulations suitable for addressing the research objectives outlined in this study.

3.1.5 Computational Methods

In ANSYS Fluent 2023 R1, spatial discretization of convective and diffusive terms is typically handled via various schemes. First-order upwind is robust and stable but diffusive, while second-order upwind improves accuracy by incorporating gradient information from upstream cells. QUICK and MUSCL are higher order alternatives, though they can introduce numerical oscillations unless used with gradient limiters. In this work, all transport equations employ the second-order upwind scheme, as it strikes a balance between solution fidelity and numerical stability, especially suitable for external bluff-body flows with moderate gradients [25].

Temporal discretization is not applicable here, given the steady-state approach of the study (for instance, transient terms are omitted). For pressure–velocity coupling, Fluent [25] offers multiple algorithms, such as SIMPLE, SIMPLEC, PISO, FSM, and Coupled. The SIMPLEC (Semi-Implicit Method for Pressure-Linked Equations–Consistent) algorithm solves the pressure and velocity fields iteratively, first guessing a velocity field to solve the momentum equations, then calculating a pressure correction from a derived Poisson-type pressure-correction equation to enforce mass conservation. This corrected pressure is subsequently used to adjust velocities, achieving a consistent solution that satisfies both momentum and continuity

equations simultaneously. Compared to the standard SIMPLE algorithm, SIMPLEC introduces modifications to the pressure-correction equation that significantly reduce numerical relaxation, thereby enhancing convergence speed by approximately 20%–30% without incurring additional memory [25]. Such characteristics are particularly advantageous in this study, where the computational domain involves complex flow patterns around building geometries, including separated regions, wake structures, and sharp pressure gradients. Furthermore, the pressure interpolation employs the PRESTO! (Pressure Staggering Option) scheme, designed specifically to improve the accuracy of pressure fields in regions of high curvature and significant pressure variations, such as those observed around roof edges and in wake zones downstream of the building geometry [25].

Residuals for all equations (continuity, momentum, turbulence) were required to drop below 10^{-4} and C_P mean value on roofs were controlled, aligning with best practice recommendations for convergence. Polynomial gradient reconstruction is performed using Fluent's least-squares cell-based method, which is optimal for unstructured and polyhedral meshes and minimizes false diffusion.

In summary, this configuration aligns closely with the setup used by Z. Liu et al. [9], who also employed second-order implicit discretization and SIMPLEC coupling to accurately resolve mean velocity and pressure profiles while maintaining computational efficiency.

Subsequently, the table 3.1 is done to collect the options selected for the simulations.

Table 3.1: Ansys Fluent Setup

General	
Type	Pressure-Based
Time	Steady
Models	
Viscous	RNG $k-\varepsilon$
Gravity	-9.81 m/s^2
Materials	
Fluid	Air
Boundary Conditions	
Inlet	Velocity-Inlet (UDF)
Internal	Interior-fluid
Outlet	Pressure-Outlet
Ground/Building	No-slip Wall
Top/Lateral	Symmetry (Slip Wall)
Sym	Symmetry Plane XY

Methods	
Scheme	SIMPLEC
Gradient	Least Squares Cell Based
Pressure	PRESTO!
Momentum	2nd Order Upwind
Turb. KE	2nd Order Upwind
Turb. Diss. Rate	2nd Order Upwind
Controls	
Pressure	0.3
Density	1
Body Forces	1
Momentum	0.7
Turb. KE	0.8
Turb. Diss. Rate	0.8
Turb. Viscosity	1
Initialization	
Method	Standard from Inlet

With the above configuration, all simulations have been carried out, depending on whether the Z. Liu et al. geometry or the study case geometry. The validated setup will now be applied in the next section to replicate the results of Z. Liu et al. [9] as a benchmark case.

3.2 Replication of Benchmark Case

3.2.1 Overview of the Study

The study conducted by Z. Liu et al. [9] investigates the aerodynamic behaviour around low-rise buildings featuring different roof configurations, namely flat roof, gable roof, and stepped roof. The research combines wind tunnel measurements using PIV with high-fidelity LES to provide detailed insights into flow separation, vortex formation, and surface pressure distributions. The building models were tested at a geometric scale of $1:200$ with a reference height $H = 60\,mm$, placed within a logarithmic ABL flow.

The key findings from Z. Liu et al.'s work can be summarized as follows:

- LES predictions closely matched PIV measurements for mean velocity and turbulence intensities, with a FAC2 exceeding 0.9 for mean velocities and less than 10% deviation in surface pressure coefficients.
- The stepped roof case introduced more complex vortex interactions compared to flat and gable roofs, resulting in higher suction regions and sharper pressure gradients.
- While LES provided superior accuracy in capturing peak loads and unsteady structures, steady RANS simulations, when properly meshed and configured, offered acceptable errors (below 15%) for mean flow predictions, making them suitable for parametric studies.

3.2.2 Geometry: Stepped Roof Case

Among the configurations analysed by Z. Liu et al., the stepped roof geometry (see figure 3.4) is selected for replication in this work due to its geometric resemblance to the industrial building studied later in this study. Both exhibit vertical discontinuities in roof elevation, which critically influence flow separation and reattachment patterns. This benchmark case enables:

1. A direct comparison between LES and steady RANS (RNG k–ε with EWT).
2. An effective transfer of validated inflow conditions, meshing strategy, and post-processing techniques to the real-scale industrial case.

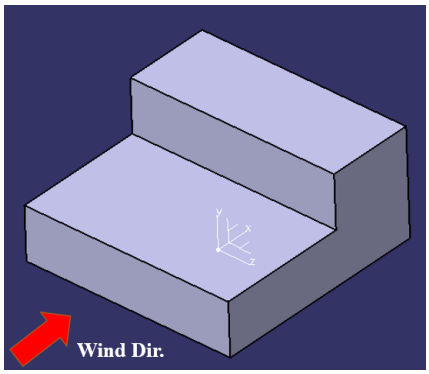

Figure 3.4: Stepped roof geometry from Z. Liu et al. [9]

3.2.3 Computational Domain

Z. Liu et al. defined the computational domain dimensions using conservative criteria, as summarized in the table below:

Table 3.2: Domain dimensions based on building height H

Direction	Extent
Upstream	$18H$
Downstream	$40H$
Lateral (each side)	$9H$
Vertical	$10H$

In the present work, however, the computational domain was constructed following the guidelines previously discussed in section 3.1.3, where the criteria established by Franke et al. [29] were adopted. This decision is based on their great acceptance in wind engineering CFD applications and the additional justification provided by more recent studies such as Abu-Zidan et al. [30], which highlight the sensitivity of flow behaviour to domain boundaries. Consequently, the chosen domain dimensions aim to ensure numerical stability, minimize artificial boundary effects, and maintain consistency with best practices for the replication of wind-induced flow phenomena. Therefore, the resulting computational domain is as shown in figure 3.5:

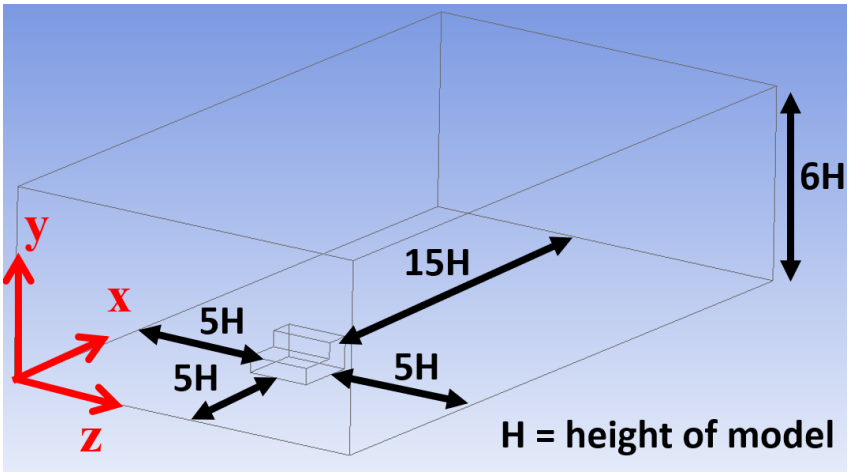

Figure 3.5: Computational domain from Z. Liu et al. [9] using the recommended guidelines [29]

The obtained final dimensions, with a height of $H = 60\ mm$, are $1.32\ m(x) \times 0.72\ m(z) \times$

$0.36\ m(y)$. The blockage ratio in this domain with the stepped roof can be calculated:

$$BR = \frac{2(30 \cdot 120) \cdot 10^{-6}\ m^2}{(0.72 \cdot 0.36)\ m^2} \times 100\% = 2.78\% < 5\%, \tag{3.15}$$

which satisfy the requirement from Tominaga et al. [28]. On the other hand, the domain was divided into two halves (symmetric plane) as justified in section 3.1.4, this means, the resulting dimensions are $1.32\ m(x) \times 0.36\ m(z) \times 0.36\ m(y)$.

3.2.4 Meshing

In accordance with the configuration and best-practice recommendations explained in section 3.1.2, it was used a structured poly-hexcore grid, looking for refinement in the near-wall regions to guarantee $y^+ \sim 1$ condition, enabling the application of EWT. To evaluate mesh sensitivity and ensure numerical consistency, a mesh convergence study was carried out using three grids of increasing resolution: *Coarse*, *Basic*, and *Fine* (see table 3.3). The geometry corresponds to the stepped roof configuration ($H = 60\,mm$), and all simulations share the same boundary conditions and numerical setup, following the methodology detailed in Section 3.1.5. Figure 3.6 shows the fine mesh from the selected study.

Table 3.3: Mesh details for coarse, basic, and fine grid configurations from Z.Liu et al. [9].

Mesh type	**Minimum size of building** (m)	**Maximum size of domain** (m)	**Height ratio of prism**	**First grid height of prism** (m)	**Estimated** y^+
Coarse grid	$6.0 \cdot 10^{-3}$ $(H/10)$	0.06	1.15	$4 \cdot 10^{-4}$	10
Basic grid	$3.0 \cdot 10^{-3}$ $(H/20)$	0.03	1.15	$4 \cdot 10^{-5}$	1
Fine grid	$1.5 \cdot 10^{-3}$ $(H/40)$	0.015	1.15	$2 \cdot 10^{-5}$	0.5

The total number of cells and the minimum surface pressure coefficient ($C_{p,\min}$) obtained along a monitored roof edge line are presented in table 3.4:

Table 3.4: Grid convergence results: total cell count and minimum pressure coefficient

Mesh Type	**Total Cells**	$\boldsymbol{C_{p,\min}}$
Coarse Mesh	66,475	–0.9286
Basic Mesh	360,282	–1.1828
Fine Mesh	2,291,689	–1.3573

From these results, it is evident that refining the mesh from *Coarse* to *Basic* leads to a sig-

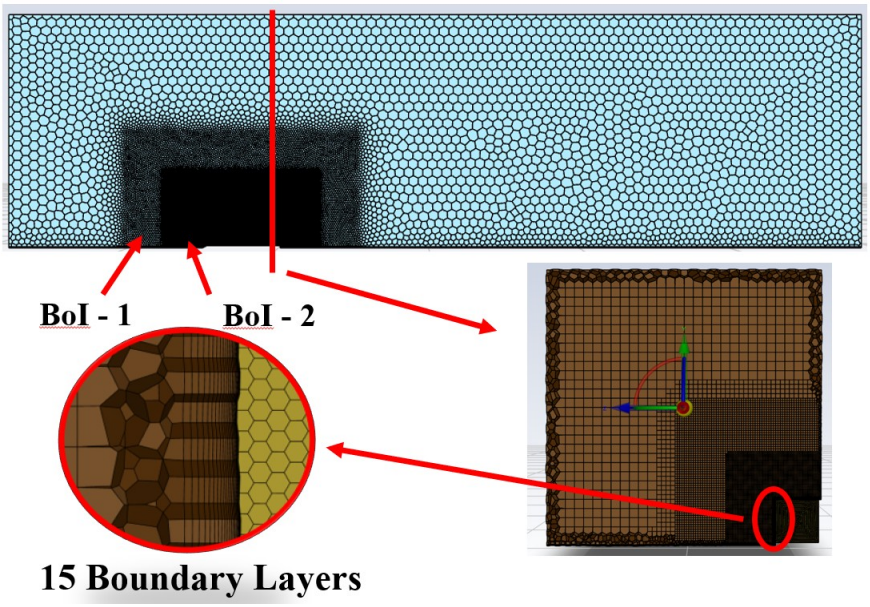

Figure 3.6: Fine Mesh from Z. Liu et al. with two BoIs

nificant variation in the minimum pressure coefficient, approximately $\sim 27\%$. However, further refinement to the *Fine* mesh results in a smaller relative change of about $\sim 15\%$, indicating the onset of asymptotic convergence.

Despite the improved accuracy, the *Fine* mesh introduces a computational cost approximately 6.4 times higher than the *Basic* mesh, with over 2 million cells. This increased resolution offers diminishing returns when compared to the added simulation time and memory demands.

Nevertheless, the *Fine* mesh has been selected for the final simulations in this thesis due to the following reasons:

- **Accuracy:** It yields the closest approximation to the asymptotic value of C_p, minimizing the underprediction of suction peaks.
- **Computational feasibility:** Although more expensive, the mesh remains within acceptable limits for the available hardware and does not compromise the project timeline.
- **Consistency:** The mesh resolution is comparable to that used by Liu et al. [9], enabling more reliable validation and comparative analysis.

In conclusion, this mesh convergence study confirms that the *Fine* mesh provides a robust and accurate numerical solution, balancing accuracy and computational feasibility, and is

therefore employed throughout this work.

Table 3.5 summarizes the quality parameters obtained for the final selected mesh (medium grid).

Table 3.5: Mesh quality metrics for the selected medium grid

Metric	Average	Minimum	Maximum	Recommended Threshold
Orthogonal Quality	0.9841	0.21569	1.0000	$> 0.1(min)$
Skewness	0.01312	0.0000	0.78431	$< 0.85(max)$
Aspect Ratio	21.1057	1.0000	555.131	$< 100(max)$

3.2.5 BC, Atmospheric Profile Validation and Methods

The following boundary conditions for the replication of the paper of Z. Liu et al. were applied:

- **Inlet:** Logarithmic velocity profile, k and ε, with parameters matched to Liu et al.: $U^*_{ABL} = 0.53\,m/s$, $y_0 = 2.04 \times 10^{-4}\,m$, and reference velocity $U_{ref} = 7.4\,m/s$ at height $y = H$. It is applied in positive X direction.
- **Ground and building walls:** No-slip condition, modelled with EWT; no explicit roughness height was assigned.
- **Top and lateral boundaries:** Treated as slip wall (symmetry).
- **Outlet:** Pressure outlet at zero gauge pressure.

These inlet values are introduced into the UDF and then interpreted, as outlined in section 3.1.4. Although the article by Z. Liu et al. employs a turbulent kinetic energy equation which is height-dependent and incorporates an intensity function (see equations 3.16), the turbulent intensity function is not available. Consequently, the Richards and Hoxey [33] equations are utilised for k and ε.

$$k(y) = \frac{3}{2}\left[U(y)I_u(y)\right]^2, \quad \varepsilon(y) = C_\mu^{3/4}\frac{k^{3/2}}{\kappa y} \tag{3.16}$$

Based on the data presented in the article, Reynolds number calculated according to authors is $\approx 2.1 \cdot 10^4$.

Prior to introducing the stepped roof geometry, the atmospheric boundary layer was validated in an empty domain using the boundary conditions and mesh described previously. The figure 3.7 shows the resulting mesh from the empty computational method, where a local sizing in the ground wall is applied.

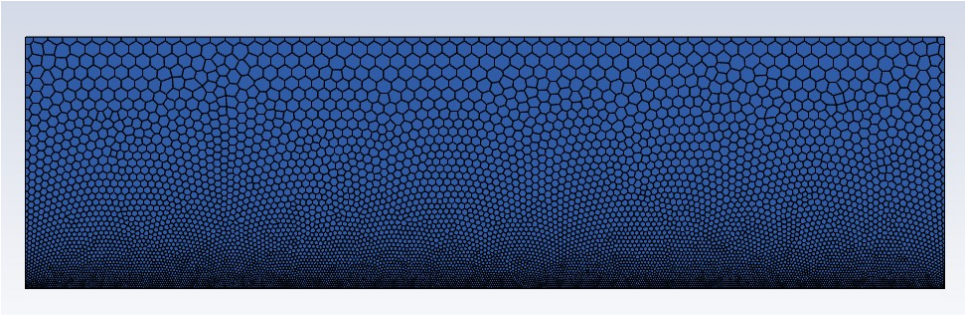

Figure 3.7: Mesh of the computational domain for the ABL Validation

The velocity profiles were extracted in four different locations along the main axis of the domain: $x/H = -4$,$x/H = 0$, $x/H = 5$ and $x/H = 14$. These velocity profiles can be seen in figure 3.8, and it is concluded its homogeneity in the computational domain.

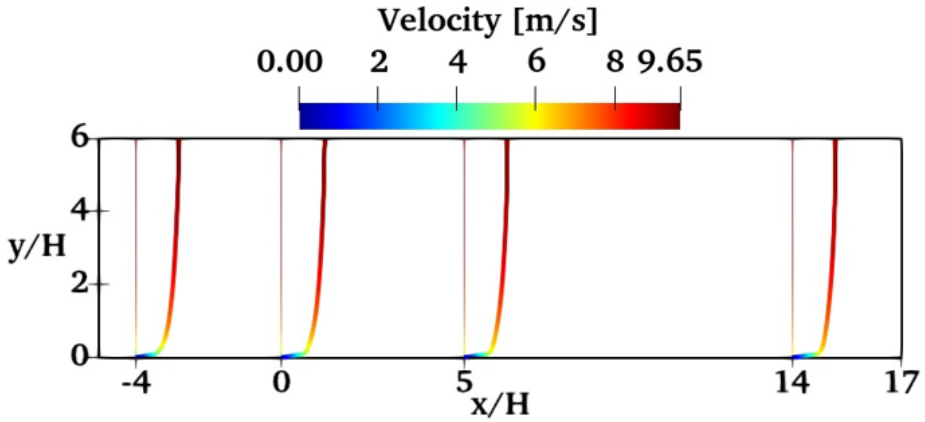

Figure 3.8: velocity profiles along the main axis of the domain: $x/H = -4$,$x/H = 0$, $x/H = 5$ and $x/H = 14$

This validation confirms that the inflow UDF and domain setup correctly reproduce the intended atmospheric conditions, and the simulation is ready to proceed with the stepped roof geometry.

In accordance with the methodologies employed in the simulation, the aforementioned elements correspond to those outlined in section 3.1.5, table 3.1.

3.3 Industrial Building Setup

3.3.1 Geometry

The studied configuration corresponds to a real stepped-roof building located in Tarragona, that has experienced wind-related issues in the past, motivating its selection for this aerodynamic analysis, as shown in figure 3.9. The structure is composed of two rectangular volumes that define the stepped-like profile: the main base and a raised upper section aligned centrally along the longitudinal axis of the domain. The total size of the model extends $200\ m$ in the streamwise direction (x), and $315\ m$ in the lateral direction (z), while the building heights are defined as $15\ m$ for the lower roof and $32\ m$ for the upper roof, both measured from the ground level. The dimensions of the upper rectangular volume are $150\ m$ in X direction and $85\ m$ for Z direction.

This stepped-roof configuration enables the formation of complex aerodynamic features such as flow separation, reattachment, and recirculating zones, particularly over the discontinuity between roof levels. Its geometric similarity to the stepped-roof case studied in Z. Liu et al. [9] facilitates a direct comparison of results under similar boundary conditions, allowing for validation of the numerical approach against established LES and experimental data.

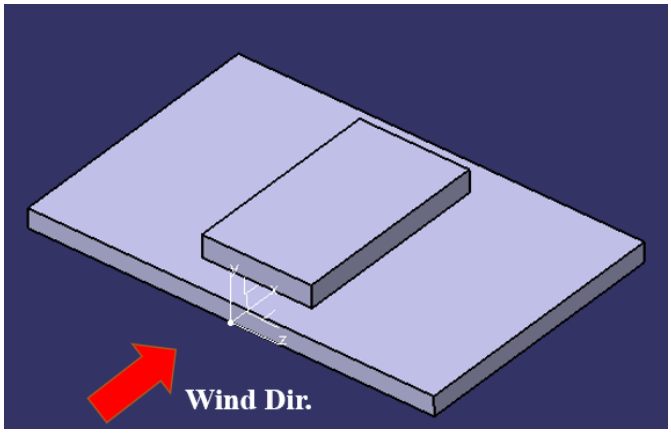

Figure 3.9: Geometry of the stepped-roof building analysed in this study.

Furthermore, as previously referenced, a scaling of the building geometry has been con-

ducted to ensure the feasibility of the simulation with the available computational resources. The dimensions of the building have been calculated to be $1 : 1000$. These are the final dimensions of the building $0.2\ m(x) \times 0.315\ m(z) \times 0.015\ m(y)$ for the base volume and $0.15\ m(x) \times 0.085\ m(z) \times 0.017\ m(y)$ for the upper section.

3.3.2 Computational Domain

In the present study, the computational domain was constructed following the guidelines previously discussed in section 3.1.3, where the criteria established by Franke et al. [29] were adopted. Therefore, the resulting computational domain is as shown in figure 3.10:

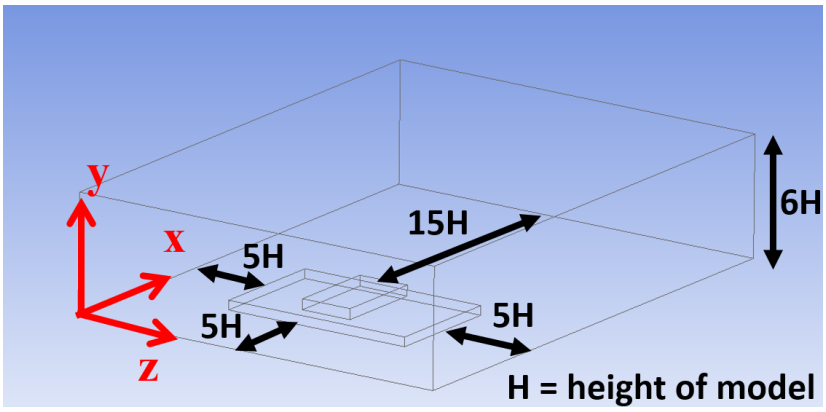

Figure 3.10: Computational domain of the geometry using the recommended guidelines [29]

The obtained final dimensions, with a height of $H = 32\ mm$, are $0.84\ m(x) \times 0.635\ m(z) \times 0.192\ m(y)$. The blockage ratio in this domain with the stepped roof can be calculated:

$$BR = \frac{(315 \cdot 15 + 85 \cdot 17) \cdot 10^{-6}\ m^2}{(0.635 \cdot 0.192)\ m^2} \times 100\% \simeq 5.06\%, \tag{3.17}$$

which satisfy the requirement from Tominaga et al. [28]. On the other hand, the domain was divided into two halves (symmetric plane) as justified in section 3.1.4, this means, the resulting dimensions are $0.84\ m(x) \times 0.318\ m(z) \times 0.192\ m(y)$.

3.3.3 Meshing

Following the setup and best-practice guidelines detailed in Section 3.1.2, a structured poly-hexcore mesh was employed, with refinement near the walls to ensure the $y^+ \sim 1$ condition, thus allowing the use of EWT. Moreover, as a meshing criterion, the variable H divided by a value such as 10, 20, 30 or 40 has been utilised. This method is widely employed in the field of building simulations. A mesh convergence study was performed using four progressively refined grids to assess mesh sensitivity and verify numerical consistency:*Coarse*, *Basic*, *Medium* and *Fine* (see table 3.6). Furthermore, two Body of Influence are added to accomplish better results near the building wall. The first one is separated from the walls $1H$ and the other one $2H$ (see figure 3.11). In order to obtain an approximate value for y^+, an estimate is derived from its definition.

$$y^+ = \frac{u_\tau y}{\nu} \Longrightarrow y = \frac{1 \cdot 1.5 \times 10^{-5}}{0.53} \approx 2.83 \cdot 10^{-5}\, m = 0.0283\, mm \tag{3.18}$$

Therefore, the first prism layer adjacent to the building walls must be set to a height of approximately $2.83 \cdot 10^{-5}\, m$ to ensure proper resolution of the viscous sublayer, as required by the EWT formulation.

Table 3.6: Mesh details for coarse, basic, medium and fine grid configurations

Mesh type	**Minimum size of building** (m)	**Maximum size of domain** (m)	**Height ratio of prism**	**First grid height of prism** (m)	**Estimated** y^+
Coarse grid	$3.2 \cdot 10^{-3}$ $(H/10)$	0.032	1.15	$2.83 \cdot 10^{-5}$	1
Basic grid	$1.6 \cdot 10^{-3}$ $(H/20)$	0.016	1.15	$2.83 \cdot 10^{-5}$	1
Medium grid	$1.1 \cdot 10^{-3}$ $(H/30)$	0.011	1.15	$2.83 \cdot 10^{-5}$	1
Fine grid	$0.8 \cdot 10^{-3}$ $(H/40)$	0.008	1.15	$2.83 \cdot 10^{-5}$	1

The mesh convergence analysis was performed by evaluating the surface pressure coefficient (C_p) at two critical locations on the rooftop of the scaled building: the upstream face ($C_{p,\text{up}}$) and the downstream face ($C_{p,\text{down}}$). The values obtained, together with the total number of cells used in each mesh configuration, are summarized in Table 3.7.

Table 3.7: Mesh convergence results based on rooftop C_p values.

Mesh	$C_{p,\textbf{up}}$	$C_{p,\textbf{down}}$	**Cell count**
Coarse	-0.3340	-0.2478	203,152
Basic	-0.3272	-0.2393	1,307,527
Medium	-0.3249	-0.2328	3,490,420
Fine	-0.3151	-0.2323	8,245,346

As the mesh is refined, a consistent reduction in the difference of C_p values is observed. Between the Basic and Medium meshes, the variation in $C_{p,\text{up}}$ is less than 1%, and between the Medium and Fine meshes, the difference further reduces to approximately 3% for $C_{p,\text{up}}$ and below 0.2% for $C_{p,\text{down}}$. These results indicate that the solution approaches mesh independence.

Despite its higher accuracy, the Fine mesh exceeds 8 million cells, significantly increasing computational time and resources. The Medium mesh, with around 3.5 million cells, yields nearly identical C_p values, particularly for the downstream surface. Therefore, the Medium mesh is chosen for the final simulations, offering a balance between accuracy and computational efficiency.

To ensure numerical stability and solution accuracy, mesh quality was evaluated using three standard metrics: orthogonal quality, skewness, and aspect ratio. Table 3.8 summarizes the quality parameters obtained for the final selected mesh (medium grid).

Table 3.8: Mesh quality metrics for the selected medium grid

Metric	**Average**	**Minimum**	**Maximum**	**Recommended Threshold**
Orthogonal Quality	0.98503	0.3005	1.0000	$> 0.1(min)$
Skewness	0.01162	0.0000	0.6995	$< 0.85(max)$
Aspect Ratio	4.78511	1.0000	97.9413	$< 100(max)$

The mesh shows great quality in the evaluated metrics. The *orthogonal quality*, with a mean value of 0.985 and a minimum above 0.3, indicates high-quality cell alignment that promotes numerical accuracy and convergence stability. *Skewness* values remain well below the critical threshold of 0.85, with a maximum of only 0.6995, ensuring minimal interpolation error and stable solver behaviour. The *aspect ratio* shows an average of 4.78, and although the maximum reaches approximately 98, it remains within acceptable limits for prism layers near walls, where high aspect ratios are common due to boundary layer stretching and probably due to the lack of resolution in the ground wall, as it is not as refined as in the building wall. Overall, the mesh

meets the recommended criteria for CFD simulations and supports the validity of the results obtained with this discretization. The final mesh can be seen in figure 3.11:

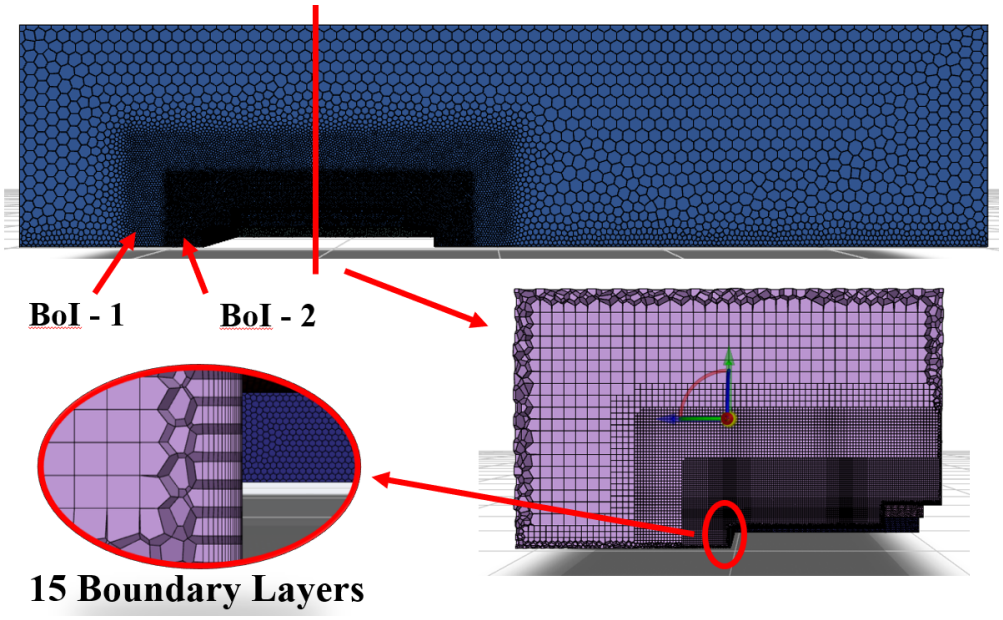

Figure 3.11: Computational medium mesh used for the simulations of the indsutrial building, with details of the BL and Body of Influence

3.3.4 BC, Atmospheric Profile Validation and Methods

In order to ensure dynamic similarity and comparability with the benchmark study by Z. Liu et al. [9], the inlet boundary conditions employed in this study replicate those of the original work. Specifically, the logarithmic velocity profile, but it was scaled by 1000 in order to maintain the values for the scaled geometry. It is defined using a friction velocity $U^*_{ABL} = 0.385 m/s$, aerodynamic roughness length $y_0 = 1.2 \cdot 10^{-5}\ m$, and a reference velocity of $U_{ref} = 7.4\ m/s$ at the building height H. Given that the stepped-roof model analysed in this study has a height of $H = 32\ mm$, the corresponding Reynolds number is computed as:

$$Re_H = \frac{U_{ref} \cdot H}{\nu} = \frac{7.4 \cdot 0.032}{1.5 \cdot 10^{-5}} \approx 15{,}787 \tag{3.19}$$

This Reynolds number is consistent with the low-turbulence, wind-tunnel-based simulations in Z.Liu et al. and remains sufficiently high to ensure the presence of turbulent separation and recirculation in the wake region. This Reynolds number ($Re_H \approx 1.6 \cdot 10^4$) falls within a

low-to-moderate turbulent regime, which is still sufficient to capture essential flow phenomena such as flow separation, recirculation behind the building, and shear layer development. While it is lower than the value used in Z.Liu et al., which reached approximately $2.1 \cdot 10^4$, it remains above the threshold commonly identified in literature for the onset of turbulence around bluff bodies [36], [37]. For instance, turbulent separation from sharp roof edges has been observed in experimental studies even for Reynolds numbers slightly above $1 \cdot 10^4$. Therefore, despite the reduced scale, the present simulation still reproduces the key aerodynamic behaviours observed in the reference study. Moreover, operating at a lower Reynolds number also contributes to enhanced numerical stability and reduced computational cost within the RANS framework.

It is to be noted that the remaining boundary conditions (outlet,ground and building walls, top and lateral boundaries) remain the same from those specified in the preceding section.

Before introducing the stepped roof geometry, the atmospheric boundary layer was validated in an empty domain using the previously described boundary conditions and mesh. The velocity profiles were extracted in four different locations along the main axis of the domain: $x/H = -4$,$x/H = 0$, $x/H = 5$ and $x/H = 14$. These velocity profiles can be seen in figure 3.12, and it is concluded its homogeneity in the computational domain.

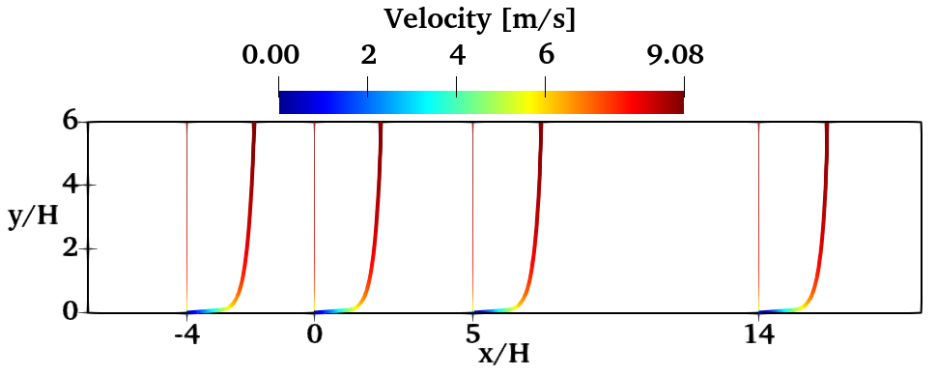

Figure 3.12: velocity profiles along the main axis of the domain: $x/H = -4$,$x/H = 0$, $x/H = 5$ and $x/H = 14$

This validation confirms that the inflow UDF and domain setup correctly reproduce the intended atmospheric conditions, and the simulation is ready to proceed with the stepped roof geometry.

In accordance with the methodologies employed in the simulation, the aforementioned elements correspond to those outlined in section 3.1.5, table 3.1.

Chapter 4

Results and Discussion

In this chapter, the results of the aforementioned simulations will be presented and discussed. The article by Z. Liu will be used as a reference study to validate the results, which will compare the same contours, velocity profiles and current lines under the same conditions. Subsequently, an analysis of the results of the industrial building will be conducted. The results of this analysis will be presented in a manner that is comparable to those of the paper.

4.1 Benchmark Case Results

To assess the accuracy and consistency of the present RANS simulations, the results were compared qualitatively with the reference LES data provided by Z. Liu et al. [9]. As no explicit numerical velocity values or pressure coefficients are given in tabular form in the article, the validation was conducted through the comparison of key graphical results, including velocity contours, streamlines, and normalized velocity profiles. In addition, the geometric scale is normalised by the height H.

Velocity Contours and Profiles

Figure 4.1 presents the comparison between the present RANS velocity contours and those reported in Fig. 16c of Liu et al. [9] for the stepped roof configuration. The velocity is normalized by the reference velocity at building height, $U_{ref} = 7.4\,m/s$.

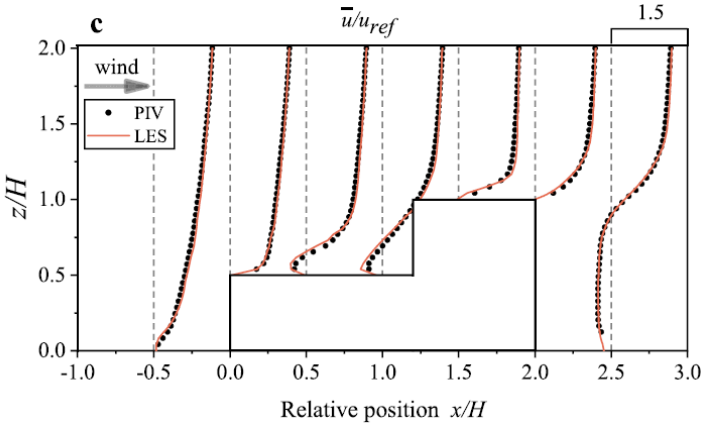

(a) Z. Liu et al. [9], LES and PIV results in mid plane

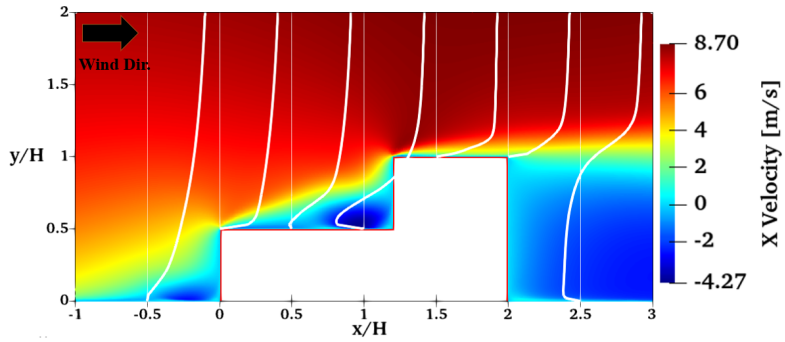

(b) Present RANS simulation showing velocity contours and profiles in the symmetry plane

Figure 4.1: Normalized velocity profiles U/U_{ref} in the vertical symmetry plane (XY).

Figure 4.1 shows a comparative representation between the current RANS-based numerical simulation and the reference data from Z. Liu et al. [9], which includes both LES simulations and experimental PIV measurements. Subfigure (a) presents vertical profiles of normalized streamwise velocity $\overline{u}/u_{ref}$ at several positions along the stepped roof geometry, whereas subfigure (b) corresponds to the present simulation's velocity contours, plotted in the same vertical plane for consistency.

From the comparison, the following observations can be made:

- **Upstream profile** ($x/H = -0.5$)**:** The RANS results match closely with LES and PIV data, showing a consistent logarithmic ABL profile before the flow interacts with the structure.
- **Above the lower roof** ($x/H = 0.5$)**:** Both the LES and RANS solutions indicate a strong acceleration over the leading edge of the lower roof, with the velocity gradient

steepening near the surface. The RANS result shows slightly more diffused gradients, typical of RANS modeling.

- **Above the lower roof ($x/H = 1$):** A big recirculation vortex is captured in both simulations. The velocity drop and delayed reattachment in the RANS contour are qualitatively consistent with LES, although the reattachment may occur slightly upstream in RANS due to known under-prediction of separation lengths in RANS models.
- **After back wall ($x/H = 2.5$):** Another bigger recirculation vortex is showed behind the building, as also presented in LES results.
- **Downstream profile ($x/H > 2.5$):** The recovery of the flow and re-establishment of the ABL profile trend is expected.

The RANS simulation accurately captures the main flow structures, including the upstream profile, flow separation at the roof step, and the development of a downstream recirculation zone.

Streamlines in Symmetry Plane

Figure 4.2 illustrates the comparison of streamline patterns in the symmetry plane for the stepped roof configuration. Subfigure (a) corresponds to the LES results reported by Z. Liu et al. [9], while subfigure (b) shows the results obtained from the present RANS simulation. Both figures clearly capture the characteristic separated shear layers and vortex structures typically associated with stepped roof geometries under ABL flow..

In both simulations, following the enumeration of present RANS results, five major flow vortices are observed:

1. **Ground-level corner vortex (V1):** Located upstream of the leading edge at $x/H \approx -0.3$, this small vortex forms due to the adverse pressure gradient and interaction of the incoming boundary layer with the building front. Both LES and RANS show good agreement in its position and scale.
2. **Lower roof corner vortex (V2):** At the step base ($x/H \approx 0.1$), a strong vortex forms due to separation at the leading edge of the lower roof. The vortex centre lies near $x/H \approx 0.5$, $y/H \approx 0.35$ in both figures, although the RANS simulation presents a slightly more

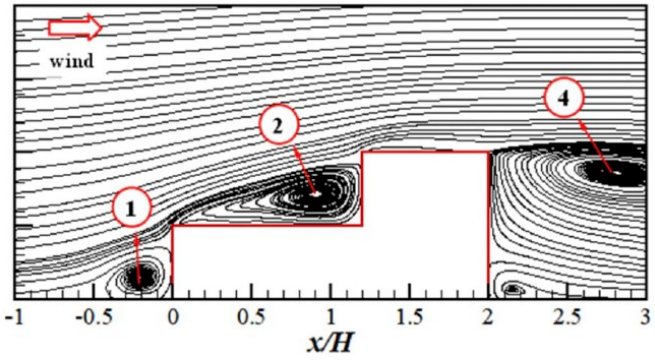

(a) Z. Liu et al. [9], LES

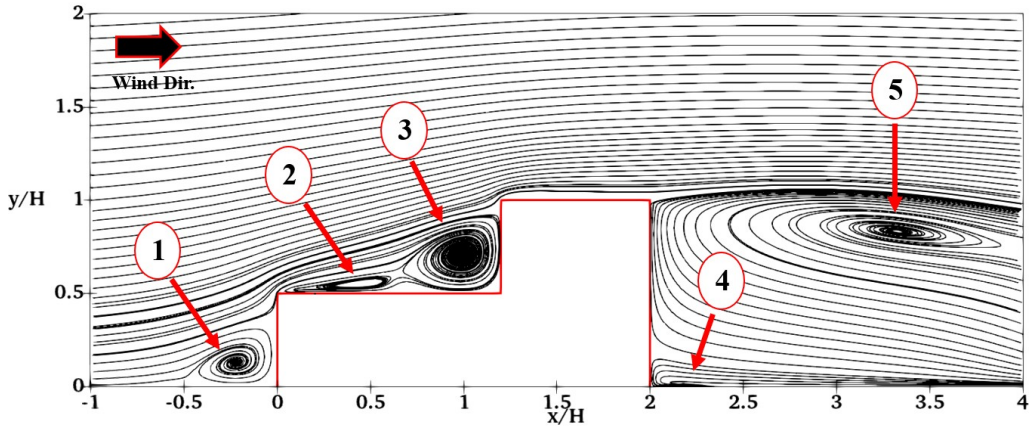

(b) Present RANS simulation

Figure 4.2: Streamlines in the symmetry plane showing flow separation and reattachment.

compact structure and it differentiates as a new vortex in RANS. Nevertheless, looking at the PIV streamlines in Z.Liu et al., RANS has greater similarity to PIV than LES.

3. **Recirculation at the upper wall (V3):** Caused by flow separation near the vertical step rise, a second vortex appears just upstream of the step-top corner at $x/H \approx 1$. This is also captured in both simulations with comparable location and curvature of streamlines, although the RANS model shows a weaker return flow.

4. **Low vortex at ground level (V4):** Observed in the RANS simulation, this structure appears around $x/H \approx 2.3$ and indicates delayed reattachment or an extended recirculation region. This feature in LES is represented more clearly, however, in PIV it is more similar to RANS.

5. **Step-down roof vortex (V5):** A large, primary recirculation vortex appears immediately downstream of the upper roof drop, starting at $x/H \approx 2.0$. The vortex core is located

around $x/H \approx 2.7$ in LES and $x/H \approx 3.3$ in RANS simulation. The shape and extent of this dominant vortex are well reproduced in the RANS simulation. The more delayed vortex observed in the RANS simulation is primarily attributed to the limited resolution of turbulent structures and flow separation, as well as higher numerical diffusion and potential limitations inherent to the turbulence model employed. Although this does not invalidate the results, it is a commonly expected behaviour when comparing RANS with LES in configurations involving sharp flow separation and a highly turbulent wake region.

Streamlines and Velocity contours in XZ Plane

Figure 4.3 illustrates the velocity field and associated streamlines in the horizontal XZ plane at pedestrian leve ($H = 0.43$), capturing the wake dynamics downstream of the stepped-roof building. Subfigure (a) correspond to the LES result from Z. Liu et al. which shows the development of two large, symmetric counter-rotating wake vortices, forming immediately after flow separation at the roof and side edges. These vortices extend downstream and dominate the wake region, highlighting the strong recirculation zone behind the structure. THis wake vortices starts at $x/H \approx 2$, having the core vortex around $x/H \approx 2.6$.

The present RANS simulation (subfigure (b)) exhibits a comparable pattern, with two coherent recirculating structures of similar size and position, starting at $x/H \approx 2$ with the core vortex at $x/H \approx 2.6$. The streamline trajectories clearly indicate flow detachment at the sharp corners of the building and subsequent reattachment downstream, replicating the general flow behaviour observed in the LES. The velocity contours indicate close to zero velocity in the wake region, with a minimal increase in speed at $z/H = 0$ and $x/H = 3$.

Although the RANS contours are smoother and the velocity deficit slightly more concentrated, this difference is expected due to the limitations of the RANS method in resolving turbulent structures and its reliance on turbulence modelling. In particular, the suppression of small-scale fluctuations and enhanced numerical diffusion in RANS contributes to a more symmetric and stable recirculation pattern.

Discussion of Results

The qualitative comparison between the present RANS simulations and the reference LES and PIV data from Z. Liu et al. [9] reveals a consistent and robust reproduction of the key aero-

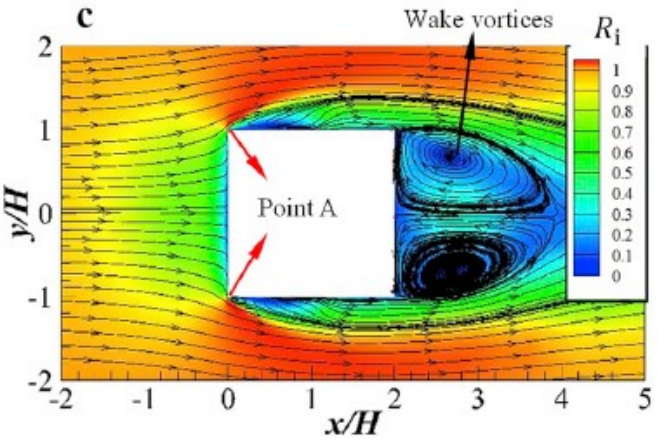

(a) Z. Liu et al. [9], LES

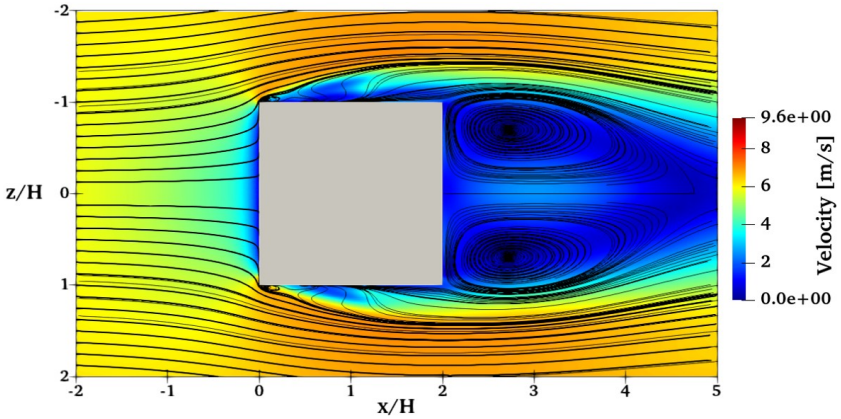

(b) Present RANS simulation

Figure 4.3: Streamlines in the XZ plane at pedestrian level ($H = 0.43$) with the velocity contour showing flow separation and recirculation.

dynamic phenomena observed around the stepped-roof building. Across the three validation figures, velocity profiles, streamlines in the symmetry plane, and XZ velocity contours, similar flow features have been identified, including boundary layer development, shear layer separation, reattachment zones, and wake vortex formation.

In particular, the ability of the RANS model to capture the different flow structures such as the corner vortices, roof separation bubbles, and wake recirculation regions confirms that, despite its lower fidelity compared to LES, the turbulence model employed is sufficient for reproducing the global behaviour of the flow. Some differences are nonetheless expected. For instance, the downstream shift in the wake vortex core position and the slightly smoother velocity gradients are consistent with the known limitations of RANS in resolving fine-scale turbulence and predicting exact reattachment points in separated flows.

It is important to note that while LES provides a more detailed view of the unsteady flow field, it comes at a significantly higher computational cost. In contrast, the RANS model used here achieves good agreement in the principal flow features with a more affordable computational effort. This trade-off between accuracy and efficiency further justifies the use of RANS for parametric or large-scale studies where qualitative flow behaviour and dominant aerodynamic effects are of great interest.

It is worth emphasizing the inherent limitations of the RNG $k - \varepsilon$ turbulence model employed. Specifically, the model's reliance on averaging turbulent fluctuations results in smoother and less detailed flow fields compared to LES, particularly in predicting the precise extent of recirculation zones and reattachment points. Nonetheless, these discrepancies remain within an acceptable margin commonly acknowledged in CFD practice, particularly for engineering studies where computational resources are limited. The purpose of this validation is thus not to achieve exact replication of the LES results but rather to confirm that the main flow structures and behaviours are correctly reproduced. Hence, despite minor quantitative deviations, the qualitative similarity observed significantly enhances the credibility and robustness of the present numerical approach.

In conclusion, the results presented demonstrate that the RANS simulations not only reproduce the expected flow physics observed in the reference LES and experimental data but also provide a reliable foundation for extending the analysis to real-world building configurations under similar boundary conditions. As a result, the numerical setup employed, from the mesh strategy, boundary conditions, and turbulence modelling approach, can be considered validated for subsequent use. The good agreement with benchmark data supports its application to the industrial building case study. Therefore, the configuration adopted in this section provides a reliable and computationally efficient framework for analysing flow behaviour around real structures with similar geometric and boundary characteristics.

4.2 Industrial Building Results: Scale $1 : 1000$

Following the validated numerical setup established in Section 4.1, this section presents the aerodynamic analysis of the industrial building using RANS simulations at a $1 : 1000$ scale. The results are organized in the following subsections to ensure consistency with the Z. Liu et al. validation, and to facilitate the identification of key aerodynamic phenomena such as boundary layer development, flow separation, vortex formation, and wake dynamics.

Velocity Contours and Profiles

Figure 4.4 presents the velocity contours of the streamwise component u in the vertical symmetry plane (XY), normalized by the reference velocity at building height, $U_{ref} = 7.4\,m/s$. White streamlines are included to highlight the main flow structures. Details a) and b) illustrate more velocity profiles in key regions. The industrial building have a stepped roof configuration with two distinct levels, which induce multiple flow separations and recirculations in the upstream and downstream regions.

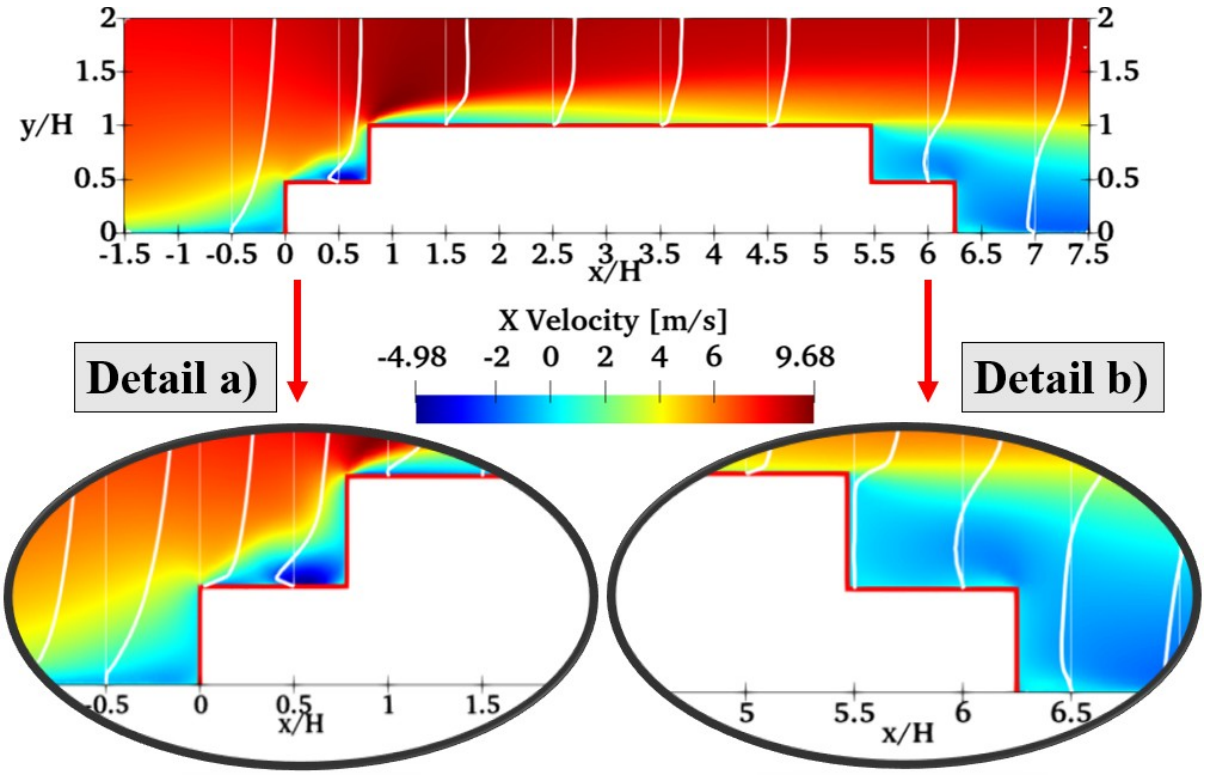

Figure 4.4: Present RANS simulation showing velocity contours and profiles in symmetry plane with Detail a) showing left profiles and Detail b) showing right profiles

Several key flow features are captured in the simulation. Upstream of the building, a typical logarithmic ABL velocity profile is observed, gradually transitioning as it approaches the first step. At the leading edge of the lower roof (figure 4.4, Detail a)), the flow separates sharply, generating a primary recirculation zone near the building wall. This recirculation core appears around $x/H \approx 0.4$ and extends up to $x/H \approx 0.7$, with reversed velocity reaching up to $u \approx -3\,m/s$.

As the flow accelerates over the lower roof, it has an impact on the second vertical wall

at $x/H \approx 5.5$, where a second major separation occurs (figure 4.4, Detail b)). The wake behind the upper roof exhibits a wide recirculation region extending from $x/H \approx 6$ to $x/H \approx 7.2$, with the vortex core located around $x/H \approx 6.7$. The reverse velocity in this region is significant, with near-zero or even negative values close to the wall. The shape and extent of this recirculating vortex are consistent with typical flow behaviour over stepped-roof buildings and align with trends seen in the Z. Liu validation.

The velocity contours also illustrate a progressive reattachment of the flow downstream, with velocity recovery becoming evident beyond $x/H > 7.5$. Above the recirculation region, the flow maintains high velocity, indeed, the acceleration at the upper roof ($x/H \approx 0.8$) approaches the maximum velocity in the domain ($u = 9.68\ m/s$), and gradually reintegrating into the outer boundary layer.

These results confirm that the simulation accurately captures the essential aerodynamic behaviour expected in this type of configuration: strong flow separation, shear layer development, and wake reattachment. The observed vortex locations and magnitudes are coherent with physical expectations and validate the fidelity of the setup under realistic boundary conditions.

Streamlines in Symmetry Plane

Figure 4.5 shows the streamlines in the vertical symmetry plane, providing detailed insight into the primary flow structures and recirculation regions induced by the stepped geometry.

In general terms, the streamline distribution clearly illustrates the complexity of the flow due to sharp edges and significant height variations of the structure. Two detailed views (Detail a) and Detail b)) are also provided to examine closely the localized vortex formations.

The main observations from the streamline analysis are:

- **Detail (a), Upstream region:** A clear vortex (V1) is identified at the lower roof edge corner, where the incoming boundary layer flow separates sharply due to the adverse pressure gradient induced by the two consecutive vertical wall. The core of this vortex is located at approximately $x/H \approx 0.6$ and extends from $x/H \approx 0.1$ to $y/H \approx 0.7$. A second (V2), smaller recirculation region is present upstream, close to the ground, at approximately $x/H \approx -0.1$. Besides, a small recirculation at the top roof appears due to the sharp roof edge.

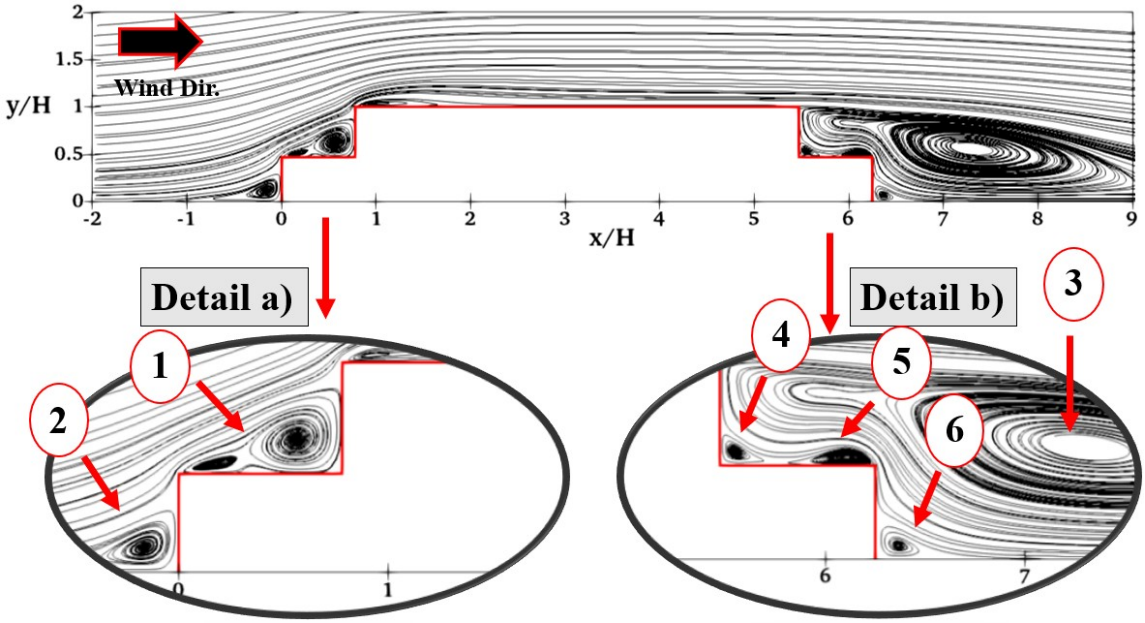

Figure 4.5: Streamlines in the vertical symmetry plane showing flow separation and vortex formations.

- **Detail (b), Downstream region:** A large recirculation zone is clearly visible in the wake behind the building (V3), starting at $x/H \approx 5.5$ and extending downstream beyond $x/H \approx 8.5$. The central vortex core is located around $x/H \approx 7.4$. The wake exhibits multiple interacting vortices due to flow separation from both the vertical and horizontal trailing edges. Additionally, smaller vortices (V4, V5) appear near the lower roof region, at approximately $x/H \approx 5.5$, and a secondary vortex (V6) close to the ground around $x/H \approx 6.2$.

The velocity contours and profiles confirms this structures, forming a closed loops near the walls, as seen in figure 4.4. The presented streamline pattern shows consistency with typical flow structures expected for stepped-roof buildings, where sharp geometry transitions result in significant separation and vortex formations. The presence and scale of these vortices strongly indicate the flow separation zones, aiding the identification of potentially problematic areas in terms of wind-induced loading and flow-induced vibrations.

Conversely, the findings reveal a composition of two geometries as outlined in Z.Liu et al., specifically the stepped roof with wind directions of $0°$ and $180°$, thereby substantiating the veracity of these results.

Wake Structures in XZ Planes at Pedestrian Level and Roof Height

Figure 4.6 displays velocity contours and streamlines at two different horizontal planes: $y/H = 0.43$, representing pedestrian level, and $y/H = 0.75$, corresponding to height over the first roof. These horizontal planes reveal significant wake structures formed due to flow interaction with the building geometry.

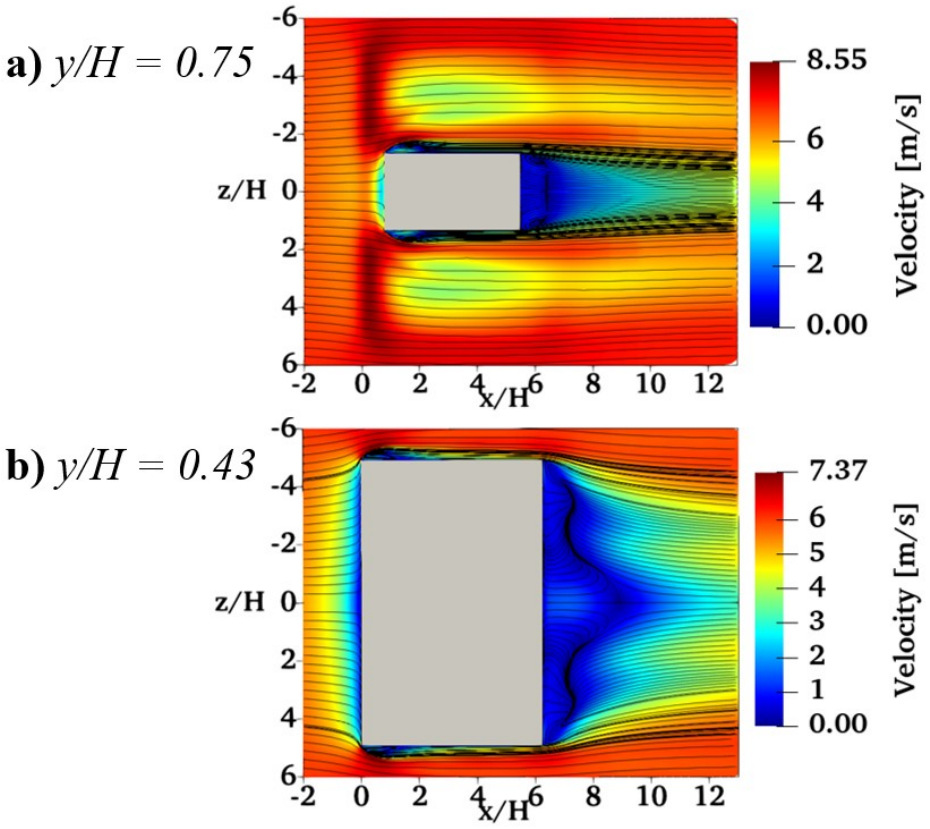

Figure 4.6: Velocity contours and streamline at (a) roof height $y/H = 0.75$, and (b) pedestrian level$y/H = 0.43$.

At roof height $y/H = 0.75$, figure 4.6a), the flow experiences clear separation around the lateral edges of the building, creating two vortices at $x/H \approx 2$, with a velocity magnitude close to $0\ m/s$. The velocity contour differentiate two symmetrical recirculation vortices extending downstream, forming a wake region. The streamline patterns indicate an elongated recirculation zone that originates immediately behind the building and extends approximately $6H$ downstream, with vortex cores approximately located at $x/H \approx 6$. Maximum velocity deficit in the wake reaches nearly zero values near the central symmetry line, progressively recovering downstream as the vortices dissipate. At $x/H \approx 0$, maximum peak velocities of

$8.55\ m/s$ occurs due to the acceleration of the lower roof.

At pedestrian level $y/H = 0.43$, figure 4.6b), similar wake characteristics are observed, although the recirculation region is broader and more elongated in the streamwise direction. This larger recirculation area extends beyond $7H$ downstream, reflecting enhanced blockage effects at lower elevations. The vortex cores shift downstream to approximately $x/H \approx 6.5$, indicating more pronounced flow blockage and greater separation. Velocity within this recirculation zone remains significantly lower compared to the free-stream region. As was also the case in the preceding results, a clear resemblance to the result obtained by Z.Liu et al. [9] can be observed in the case of a stepped roof with wind direction of $180\circ$.

In summary, both horizontal planes effectively highlight substantial wake formation and flow separation due to the building geometry, characterized by symmetrical vortices (as a limitation of RANS) and substantial velocity deficits. The increased extension of the wake region at pedestrian level underscores the importance of assessing pedestrian-level comfort in urban environments, while the clearly defined vortices at roof height illustrate the dominant influence of the roof edge geometry in generating turbulent wake structures.

Three-Dimensional Flow and Pressure Coefficients

Figure 4.7 illustrates the three-dimensional streamline patterns around the industrial building, superimposed with the distribution of C_p on its building surfaces. As discussed previously, the three-dimensional streamlines provide a comprehensive visualization of flow structures, clearly revealing the intricate patterns of separation, recirculation, and reattachment.

Specifically, upstream flow separates at the sharp leading edges of both building steps, generating distinctive recirculation vortices along the roof surfaces. These vortices significantly influence local pressure distributions, resulting in prominent low-pressure (suction) regions. The highest suction occurs at the upper leading edges, reaching minimum pressure coefficients around $C_p \approx -2.1$. Such strong suction indicates critical areas susceptible to wind-induced uplift and fatigue stresses, as highlighted in similar studies by Blocken et al.[24] and Tominaga et al.[8].

Conversely, high-pressure regions ($C_p \approx 0.6$) are observed at the windward facade and the lower leading edges, caused by the direct contact and stagnation of the incoming airflow. These elevated pressure zones represent significant structural loading, emphasizing the need

for careful consideration in the structural design phase.

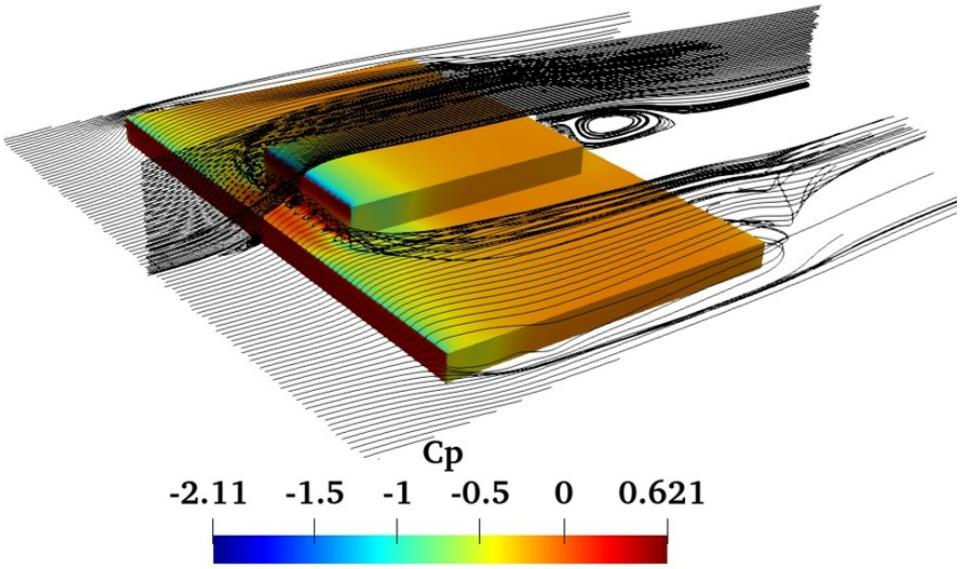

Figure 4.7: Three-dimensional streamlines and surface pressure coefficient distribution around the building walls.

To contextualise the pressure coefficients obtained in the present simulation, a comparison is made with the experimental data reported by Aldoum et al. [38], who investigated stepped-roof buildings under wind tunnel conditions. Their study measured peak negative C_p on the roof surfaces, reporting typical values in the range of -1.0 to -1.2 near the roof steps and on the leeward faces for 0° wind incidence.

In contrast, the current RANS simulation yields a peak suction value of $C_p = -2.11$ and a maximum positive pressure of $C_p = 0.6$ on the windward facade. While the positive pressure coefficient agrees well with common literature for frontal contact zones, the negative peak is considerably more intense than the range observed in wind tunnel measurements. This difference can be explained with the following factors:

- The sharper geometry and abrupt vertical steps in the simulated building enhance local flow separation, intensifying suction at the edges.
- RANS turbulence models, while effective in capturing general flow structures, may overestimate peak suction zones due to their inability to resolve small-scale turbulent fluctuations.
- The inflow boundary conditions differ significantly: the present simulation is based on a numerically prescribed ABL profile with a reference velocity of $U = 7.4\,m/s$, while

Aldoum et al. [38] used a wind tunnel setup with different roughness and turbulence characteristics. These differences can strongly influence local pressure distributions.

Nevertheless, the order of magnitude remains consistent, and the qualitative distribution of pressure aligns well with expected aerodynamic behaviour.

Flow Topology and λ_2 Criterion

To further characterise the three-dimensional vortex structures developing around the stepped-roof industrial building, the λ_2 criterion [39] is employed. Figure 4.8 shows an isosurface at $\lambda_2 = 10^4$, coloured by the velocity magnitude. The λ_2 method identifies coherent vortex cores by locating minimums of pressure, and is particularly suitable for detecting strong vortical structures in incompressible flows.

In this figure 4.8, several high-energy vortices are observed, predominantly near the leading edge of the elevated roof step and along the sides of the building. The vortical structures take the form of elongated tubes, wrapping around the building geometry and extending downstream, indicating the presence of strong, coherent flow separation followed by intense streamwise vorticity.

Of particular interest is the structure developing at the windward base of the upper roof, where the incoming flow separates and bends around the step corner. This forms a prominent three-dimensional vortex wrapping around the building edges, consistent with the known *horseshoe vortex system* described in Z. Liu et al. [9]. These vortices originate due to the interaction between the ground-attached boundary layer and the frontal face of the stepped geometry, leading to the formation of recirculating vortex that remain attached to the base and roof edge.

The flow reattaches at the top surface after the step, and another set of arch-shaped vortices develop further downstream as the flow accelerates around the sidewalls. The coloured velocity magnitude reveals that the vortex cores are associated with regions of high kinetic energy, reaching values close to 9–$10\,m/s$, while their outer layers decay.

These features highlight the complex three-dimensionality of the flow, complementing the streamline and pressure coefficient analyses discussed previously. The identification of such structures provides valuable insight into the onset of flow-induced vibrations, local suction

zones, and potential areas of wind loading amplification, especially relevant in structural design and ventilation studies.

While the main vortex structures observed in this simulation align with those identified by Z. Liu et al. [9], some differences must be acknowledged due to the different turbulence modelling strategies. The reference study employed LES, In contrast, the present study is based on RANS modelling. As a result, the vortices visualised here appear more coherent and stable, and their downstream evolution is less chaotic compared to LES.

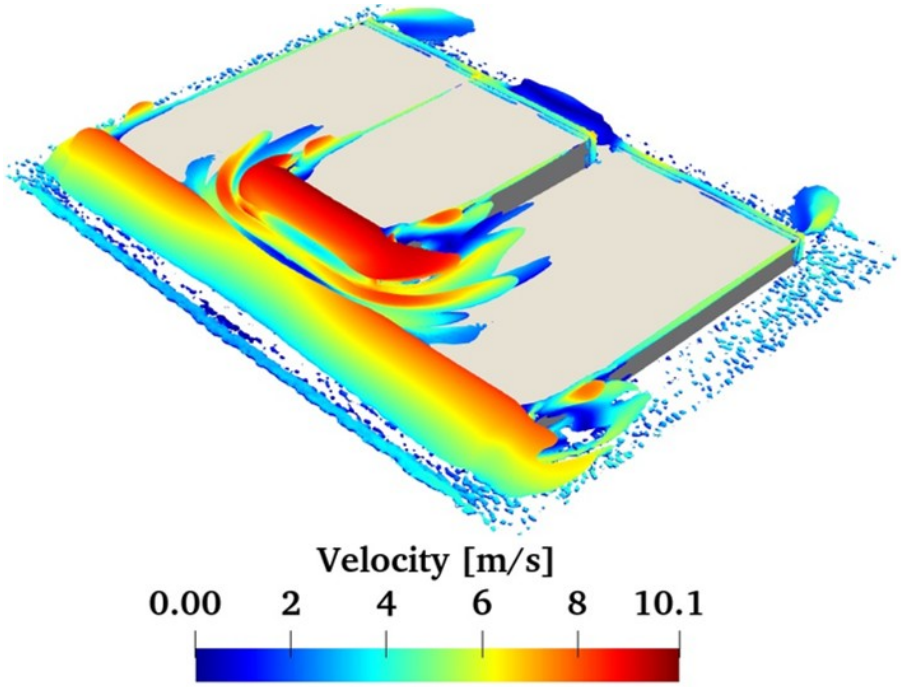

Figure 4.8: Isosurface of $\lambda_2 = 10^4$ coloured by velocity magnitude.

Discussion of Results

The results obtained from the RANS simulation of the industrial building at a scale of $1:1000$ provide a comprehensive and coherent aerodynamic analysis, highlighting critical flow features that significantly influence wind-induced loading on stepped-roof structures. The findings presented through velocity contours, streamline visualizations, pressure distributions, and vortex topology demonstrate a consistent and physically plausible behaviour of the airflow around the building.

Velocity contours in the symmetry plane reveal distinct separation and recirculation pat-

terns induced by the stepped geometry, closely aligning with general aerodynamic phenomena expected for stepped-roof configurations, such as those described by Z.Liu et al. [9]. Notably, significant flow separations are captured at both the leading edges of the lower and upper roof sections. These separation zones result in intense localized recirculations, with reverse flow velocities reaching magnitudes up to approximately $-3\ m/s$. Furthermore, a robust wake structure extends downstream, exhibiting reattachment and velocity recovery in a realistic manner consistent with previously validated studies.

Analysis of the streamline patterns reinforces these observations by distinctly capturing vortical structures, particularly the prominent recirculation regions upstream (Detail a)) and downstream (Detail b)) of the building. The presence and relative positioning of these vortices (V1 to V6) clearly align with known flow behaviours reported in the literature for similar stepped-roof geometries. The detailed vortex analysis highlights the complexity introduced by sharp edges and stepped heights, emphasizing potential issues related to wind-induced vibrations and dynamic loading.

The horizontal wake analysis at pedestrian and roof heights further confirms the significant influence of building geometry on the downstream flow patterns. At pedestrian level, the extended recirculation region emphasizes the importance of evaluating pedestrian comfort and safety in urban environments, given the substantial blockage effects observed. Similarly, at roof height, clearly defined symmetrical vortices demonstrate the importance of stepped-roof geometry in shaping wake dynamics, consistent with findings reported in Z. Liu et al. [9] for stepped-roof configurations at different wind directions.

The three-dimensional visualization of flow structures using streamline and pressure coefficient distributions further supports the aforementioned analyses. Peak suction pressures reaching values of $C_p = -2.11$ are notably higher compared to experimental wind tunnel measurements by Aldoum et al. [38], who reported peak negative pressure coefficients around -1.2 for similar stepped-roof configurations. This discrepancy likely results from the more abrupt geometry, enhanced flow separations, and inherent limitations of RANS modelling, which tends to amplify peak suction values by underestimating small-scale turbulence dissipation. Nevertheless, positive pressures recorded at the windward façade ($C_p = 0.6$) remain consistent with literature results.

The use of the λ_2 criterion further clarifies the three-dimensional vortex topology. Large horseshoe vortices, similar to those described by Liu et al. [9], confirm the presence of complex, coherent vortical structures around sharp edges and corners. These structures, although more

stable and coherent in RANS than in LES, affirm the physical accuracy of the simulation and provide valuable insights for structural and aerodynamic design considerations.

Overall, the results presented in this study effectively validate the application of the RANS modelling approach for evaluating wind effects on stepped-roof industrial buildings. Despite known limitations in resolving fine-scale turbulence, the methodology captures dominant aerodynamic phenomena, offering practical results into critical wind loading areas and phase structural optimization design. The consistency of flow behaviour observed in the validated Z.Liu et al. simulations further substantiates confidence in the present numerical framework.

Chapter 5

Conclusions and future work

This study investigated the aerodynamic behaviour of a stepped-roof industrial building under atmospheric boundary layer (ABL) conditions using computational fluid dynamics (CFD). The simulation setup was first validated against the reference case by Z. Liu et al. [9], confirming that the chosen steady RANS approach with the RNG k-ε turbulence model and Enhanced Wall Treatment (EWT) accurately reproduces key aerodynamic features observed in experimental and LES studies.

The objectives outlined in Chapters 1 and 2, identifying major flow structures and validating the numerical approach, were successfully achieved. The main findings can be summarized as follows:

- The flow simulation reproduced major separation and recirculation regions both upstream and downstream of the building steps, closely matching those observed in the validated stepped-roof configuration.
- High velocity gradients and flow acceleration near the roof edges were observed, with peak values reaching approximately $9.68\ m/s$. These results suggest zones of elevated aerodynamic loading that require special attention in design stages.
- Surface pressure analysis revealed critical suction areas on the upper roof with a minimum pressure coefficient of $C_p = -2.11$. Although higher than typical values found in experimental studies, this magnitude is consistent with the sharp geometry and the limitations of steady RANS modelling, as discussed in previous chapter.
- Three-dimensional vortex structures, visualised using the λ_2 criterion, revealed coherent

horseshoe-type vortices and streamwise structures wrapping around roof edges. These findings are consistent with flow topologies reported in literature, validating the physical interpretation of the flow.

These results confirm that the numerical setup is robust, efficient, and capable of capturing the dominant aerodynamic effects in low-rise stepped-roof buildings under realistic wind conditions. The methodology demonstrated here can serve as a valuable tool for early-stage engineering evaluations, especially in practical cases where LES or wind tunnel testing is not feasible.

Future Work

While the current work provides a solid starting point, several approaches exist for improving and extending the study:

- **Transient simulations:** Employing LES or hybrid RANS-LES approaches would allow better resolution of unsteady flow characteristics, turbulent structures, and fluctuating forces.
- **Parametric studies:** Analysing the effects of varying wind directions, stepped roof ratios, or environmental boundary conditions could generalize the conclusions to a broader range of industrial building designs.
- **Mitigation strategies:** Investigating geometrical modifications or passive control techniques aimed at reducing suction peaks and flow separation could contribute to safer, more efficient structural designs.
- **Experimental validation:** Complementing the simulations with wind tunnel testing under comparable conditions would further reinforce the validity of the numerical results and refine turbulence modelling strategies.

In conclusion, the study meets its original objectives by delivering a validated and insightful aerodynamic assessment of a realistic industrial building configuration. The numerical methodology adopted offers a practical compromise between accuracy and computational cost and opens the door for more advanced future studies that could support both structural safety and urban design optimization.

Bibliography

[1] Y. Uematsu and N. Isyumov, "Wind pressures acting on low-rise buildings," *Journal of Wind Engineering and Industrial Aerodynamics*, vol. 82, pp. 1–25, 1999.

[2] X. Zheng, H. Montazeri, and B. Blocken, "Cfd simulations of wind flow and mean surface pressure for buildings with balconies: Comparison of rans and les," *Building and Environment*, vol. 173, Apr. 2020, ISSN: 03601323. DOI: 10.1016/j.buildenv.2020.106747.

[3] M. F. Khaled and A. M. Aly, *Assessing aerodynamic loads on low-rise buildings considering reynolds number and turbulence effects: A review*, Dec. 2022. DOI: 10.1186/s42774-022-00114-0.

[4] NSF. The National Science Foundation (NSF), *Network, and structural extreme events reconnaissance (steer)*, https://web.fulcrumapp.com/apps/be73ae35-9ca8-43dd-aaff-469cc348ffed, Accessed: 2025-06-25, 2019.

[5] G. L. Larose and A. D'Auteuil, "On the reynolds number sensitivity of the aerodynamics of bluff bodies with sharp edges," *Journal of Wind Engineering and Industrial Aerodynamics*, vol. 94, pp. 365–376, 5 May 2006, ISSN: 01676105. DOI: 10.1016/j.jweia.2006.01.011.

[6] Y. Jia, B. L. Sill, and T. A. Reinhold, "Effects of surface roughness element spacing on boundary-layer velocity profile parameters," Tech. Rep., 1998, pp. 215–230.

[7] J. D. H. A', M. J. Syme, and M. Kasperski, "Optimised design of a low-rise industrial building for wind loads," *Journal of Wind Engineering and Industrial Aerodynamics*, vol. 57, pp. 391–401, 1995.

[8] Y. Tominaga, S. ichi Akabayashi, T. Kitahara, and Y. Arinami, "Air flow around isolated gable-roof buildings with different roof pitches: Wind tunnel experiments and cfd simulations," *Building and Environment*, vol. 84, pp. 204–213, Jan. 2015, ISSN: 03601323. DOI: 10.1016/j.buildenv.2014.11.012.

[9] Z. Liu, Z. Yu, X. Chen, R. Cao, and F. Zhu, "An investigation on external airflow around low-rise building with various roof types: Piv measurements and les simulations," *Building and Environment*, vol. 169, Feb. 2020, ISSN: 03601323. DOI: 10.1016/j.buildenv.2019.106583.

[10] A. M. Aly, "Atmospheric boundary-layer simulation for the built environment: Past, present and future," *Building and Environment*, vol. 75, pp. 206–221, 2014, ISSN: 03601323. DOI: 10.1016/j.buildenv.2014.02.004.

[11] M. A. Mooneghi, P. Irwin, and A. G. Chowdhury, "Partial turbulence simulation method for predicting peak wind loads on small structures and building appurtenances," *Journal of Wind Engineering and Industrial Aerodynamics*, vol. 157, pp. 47–62, Oct. 2016, ISSN: 01676105. DOI: 10.1016/j.jweia.2016.08.003.

[12] T. Stathopoulos, "Wind loads on low buildings: A review of data from the past decade," *Building and Environment*, vol. 44, no. 4, pp. 912–921, 2009. DOI: 10.1016/j.buildenv.2008.06.015.

[13] N. Abdelfatah, A. Elawady, P. Irwin, and A. G. Chowdhury, "Experimental investigation of wind impact on low-rise elevated residences," *Engineering Structures*, vol. 257, Apr. 2022, ISSN: 18737323. DOI: 10.1016/j.engstruct.2022.114096.

[14] H. Montazeri and B. Blocken, "Cfd simulation of wind-induced pressure coefficients on buildings: Validation and impact of numerical parameters," *Building and Environment*, vol. 72, pp. 189–204, 2014. DOI: 10.1016/j.buildenv.2013.11.004.

[15] B. Blocken, "50 years of computational wind engineering: Past, present and future," *Journal of Wind Engineering and Industrial Aerodynamics*, vol. 129, pp. 69–102, 2014. DOI: 10.1016/j.jweia.2014.03.008.

[16] M. Shirzadi, P. Mirzaei, and Y. Tominaga, "Cfd analysis of cross-ventilation flow in a group of generic buildings: Comparison between steady rans, les and wind tunnel experiments," *Journal of Wind Engineering and Industrial Aerodynamics*, vol. 195, p. 104 012, 2020. DOI: 10.1016/j.jweia.2020.104012.

[17] T. van Hooff, B. Blocken, and Y. Tominaga, "On the accuracy of cfd simulations of cross-ventilation flows for a generic isolated building: Comparison of rans, les and experiments," *Building and Environment*, vol. 114, pp. 148–165, 2017. DOI: 10.1016/j.buildenv.2016.12.019.

[18] M. Haines and I. Taylor, "Numerical investigation of the flow field around low rise buildings due to a downburst event using large eddy simulation," *Journal of Wind Engineering and Industrial Aerodynamics*, vol. 172, pp. 12–30, Jan. 2018, ISSN: 01676105. DOI: 10.1016/j.jweia.2017.10.028.

[19] P. Sagaut, *Large Eddy Simulation for Incompressible Flows: An Introduction*, 3rd. Springer, 2006.

[20] H. Lübcke, M. Schmidt, T. Rung, and F. Thiele, "Comparison of les and rans in bluff-body flows," *Journal of Wind Engineering and Industrial Aerodynamics*, vol. 89, pp. 1471–1485, 2001. DOI: 10.1016/S0167-6105(01)00134-9.

[21] J. Larsson and Q. Wang, "The prospect of using les and des in engineering design, and the research required to get there," *AIAA Journal*, vol. 52, no. 11, pp. 2341–2355, 2014. DOI: 10.2514/1.J052790.

[22] M. F. Khaled and A. M. Aly, "Augmenting external surface pressures' predictions on isolated low-rise buildings using cfd simulations," *Wind and Structures*, vol. 37, no. 4, pp. 255–274, 2023. DOI: 10.12989/was.2023.37.4.255.

[23] A. M. Aly and H. Gol-Zaroudi, "Peak pressures on low rise buildings: Cfd with les versus full scale and wind tunnel measurements," *Wind and Structures*, vol. 30, no. 1, pp. 99–117, 2020. DOI: 10.12989/was.2020.30.1.099.

[24] B. Blocken, "Cfd simulation of building aerodynamics: Accurate, practical and reliable?" *Building and Environment*, vol. 84, pp. 1–10, 2015. DOI: 10.1016/j.buildenv.2014.09.012.

[25] ANSYS, Inc., *Ansys fluent theory guide*, ANSYS Fluent Release 2023 R1, ANSYS, Inc., Canonsburg, PA, USA, 2023. [Online]. Available: https://www.ansys.com/products/fluids/ansys-fluent.

[26] J. H. Ferziger and M. Perić, *Computational Methods for Fluid Dynamics*, 2nd. Berlin, Heidelberg: Springer, 2002, See especially pp. 68–74 for mesh quality metrics, and pp. 85–90 for convergence and numerical stability discussion, ISBN: 978-3-540-42074-3.

[27] M. Sosnowski, R. Gnatowska, J. Sobczyk, and W. Wodziak, "Computational domain discretization for cfd analysis of flow in a granular packed bed," *Journal of Theoretical and Applied Mechanics*, vol. 57, pp. 833–842, Oct. 2019. DOI: 10.15632/jtam-pl/112017.

[28] Y. Tominaga, A. Mochida, R. Yoshie, *et al.*, "Aij guidelines for practical applications of cfd to pedestrian wind environment around buildings," *Journal of Wind Engineering and Industrial Aerodynamics*, vol. 96, pp. 1749–1761, 10-11 Oct. 2008, ISSN: 01676105. DOI: 10.1016/j.jweia.2008.02.058.

[29] J. Franke, A. Hellsten, H. Schlünzen, and B. Carissimo, "Best practice guideline for the cfd simulation of flows in the urban environment," in *COST Action 732 Report*, 2007. [Online]. Available: https://www.mi.uni-hamburg.de/fileadmin/files/forschung/meteorologie/dokumente/cost/cfdguide.pdf.

[30] Y. Abu-Zidan, P. Mendis, and T. Gunawardena, "Optimising the computational domain size in cfd simulations of tall buildings," *Heliyon*, vol. 7, 4 Apr. 2021, ISSN: 24058440. DOI: 10.1016/j.heliyon.2021.e06723.

[31] J. Singh and A. K. Roy, "Cfd simulation of the wind field around pyramidal roofed single-story buildings," *SN Applied Sciences*, vol. 1, 11 Nov. 2019, ISSN: 25233971. DOI: 10.1007/s42452-019-1476-2.

[32] C. K. Choi, D. K. Kwon, F. L. Haan, and A. Kareem, "Effect of blockage on wind tunnel modelling of buildings," *Journal of Wind Engineering and Industrial Aerodynamics*, vol. 77-78, pp. 531–541, 1998. DOI: 10.1016/S0167-6105(98)00187-2.

[33] P. Richards and R. Hoxey, "Appropriate boundary conditions for computational wind engineering models using the k–e turbulence model," *Journal of Wind Engineering and Industrial Aerodynamics*, vol. 46-47, pp. 145–153, 1993. DOI: 10.1016/0167-6105(93)90124-7.

[34] B. Blocken, T. Stathopoulos, and J. Carmeliet, "Cfd simulation of the atmospheric boundary layer: Wall function problems," *Atmospheric Environment*, vol. 41, pp. 238–252, 2 Jan. 2007, ISSN: 13522310. DOI: 10.1016/j.atmosenv.2006.08.019.

[35] L. S. Cochran, "Atmospheric boundary layer modeling in wind engineering: Development and limitations," *Journal of Wind Engineering and Industrial Aerodynamics*, vol. 93, no. 3, pp. 173–189, 2005. DOI: 10.1016/j.jweia.2004.12.006.

[36] S. Murakami, "Comparison of various turbulence models applied to a bluff body," *Journal of Wind Engineering and Industrial Aerodynamics*, vol. 46-47, pp. 21–36, 1993. DOI: 10.1016/0167-6105(93)90274-6.

[37] A. W. Julian C. R. Hunt and P. Moin, "Eddies, streams, and convergence zones in turbulent flows around obstacles," *Proceedings of the Royal Society of London. Series A, Mathematical and Physical Sciences*, vol. 356, no. 1686, pp. 227–253, 1978. DOI: 10.1098/rspa.1977.0147.

[38] M. Aldoum, T. Stathopoulos, J. Chavez, and A. Baskaran, "Exploring the impact of vertically separated flows on wind loads of stepped-roof buildings," *Frontiers in Physics*, vol. 11, p. 1 225 817, 2023. DOI: 10.3389/fphy.2023.1225817. [Online]. Available: https://www.frontiersin.org/articles/10.3389/fphy.2023.1225817/full.

[39] J. Jeong and F. Hussain, "On the identification of a vortex," *Journal of Fluid Mechanics*, vol. 285, pp. 69–94, 1995. DOI: 10.1017/S0022112095000462.

Appendix A

Fluent UDF Scripts

The following sections describe de used UDF for the ABL profile applied in the inlet boundary condition for both Z.Liu et al. and Industrial Building simulations.

A.1 Z.Liu et al. UDF

Fluent UDF

```
#include "udf.h"

float ref_vel = 7.4; /* VElocidad de referencia */
float friction_vel = 0.53; /* Velocidad de friccion */
float roughness = 0.000204; /* Rugosidad del suelo */

/* DEFINICION DEL PERFIL DE VELOCIDAD HORIZONTAL DEL VIENTO */

DEFINE_PROFILE(velocidad_viento, zona, indice_var)
{
    face_t cara;
    float coord[ND_ND];

    begin_f_loop(cara, zona)
    {
        F_CENTROID(coord, cara, zona);
        F_PROFILE(cara, zona, indice_var) = (friction_vel / 0.41) * log((
            coord[1] + roughness) / roughness);
```

```
    }
    end_f_loop(cara, zona)
}

/* DEFINICION DEL PERFIL DE E. CINETICA TURBULENTA */

DEFINE_PROFILE(energia_cinetica_turb, zona, indice_var)
{
    face_t cara;
    float coord[ND_ND];

    begin_f_loop(cara, zona)
    {
        F_CENTROID(coord, cara, zona);
        F_PROFILE(cara, zona, indice_var) = 3.33 * (friction_vel *
            friction_vel);
    }
    end_f_loop(cara, zona)
}

/* DEFINICION DEL PERFIL DE TASA DE DISIPACION TURBULENTA */

DEFINE_PROFILE(disp_turbulenta, zona, indice_var)
{
    face_t cara;
    float coord[ND_ND];

    begin_f_loop(cara, zona)
    {
        F_CENTROID(coord, cara, zona);
        F_PROFILE(cara, zona, indice_var) = (friction_vel * friction_vel *
            friction_vel) / (0.41 * (coord[1] + roughness));
    }
    end_f_loop(cara, zona)
}
```

A.2 Industrial Building UDF

Fluent UDF

```
#include "udf.h"

float ref_vel = 7.4; /* velocidad de modelo y prototipo*/
float friction_vel = 0.385; /* velocidad de la capa límite (fricción)
   escalada 1/1000 del paper de Zhixiang-Liu 2020*/
float roughness = 1.2e-5; /*rugosidad escalada 1/1000 del paper */


/* DEFINICION DEL PERFIL DE VELOCIDAD HORIZONTAL DEL VIENTO */

DEFINE_PROFILE(velocidad_viento, zona, indice_var)
{
    face_t cara;
    float coord[ND_ND];

    begin_f_loop(cara, zona)
    {
        F_CENTROID(coord, cara, zona);
        F_PROFILE(cara, zona, indice_var) = (friction_vel / 0.41) * log((
            coord[1] + roughness) / roughness);
    }
    end_f_loop(cara, zona)
}

/* DEFINICION DEL PERFIL DE E. CINETICA TURBULENTA */

DEFINE_PROFILE(energia_cinetica_turb, zona, indice_var)
{
    face_t cara;
    float coord[ND_ND];

    begin_f_loop(cara, zona)
    {
        F_CENTROID(coord, cara, zona);
        F_PROFILE(cara, zona, indice_var) = 3.33 * (friction_vel *
            friction_vel);
    }
    end_f_loop(cara, zona)
}
```

```
/* DEFINICION DEL PERFIL DE TASA DE DISIPACION TURBULENTA */

DEFINE_PROFILE(disp_turbulenta, zona, indice_var)
{
    face_t cara;
    float coord[ND_ND];

    begin_f_loop(cara, zona)
    {
        F_CENTROID(coord, cara, zona);
        F_PROFILE(cara, zona, indice_var) = (friction_vel * friction_vel *
            friction_vel) / (0.41 * (coord[1] + roughness));
    }
    end_f_loop(cara, zona)
}
```